Experiments with Trapped Ions: Entanglement, Novel Traps, and Quantum Jumps

Jennifer F. Lilieholm

A dissertation
submitted in partial fulfillment of the
requirements for the degree of

Doctor of Philosophy

University of Washington

2020

Reading Committee:

Boris B. Blinov, Chair

Subhadeep Gupta

Stephen Sharpe

Program Authorized to Offer Degree:
Physics

University of Washington

Abstract

Experiments with Trapped Ions: Entanglement, Novel Traps, and Quantum Jumps

Jennifer F. Lilieholm

Chair of the Supervisory Committee:
Title of Chair Boris B. Blinov
Physics

Quantum computing promises to revolutionize modern computation. The race to establish a reliable quantum computing system has spurred research over the globe with the goal of establishing a reliable qubit system. One of the more promising candidates are trapped ions. To that end, I have characterized, improved, and designed experiments to be performed in a novel parabolic mirror ion trap. We measured the trap to have a light collection efficiency of 39%, nearly an order of magnitude higher than the light collection of ion traps utilizing standard collection optics. The parabolic mirror also improves the quality of image collected from a trapped ion, but is limited by the micromotion the ion undergoes while at the optical focus. We designed a new trap component to allow radial control over the ion position by moving the RF null, instead of displacing it with DC bias plates.

This improved trapping system is a key part of our plan to to remotely entangle an In donor defect in ZnO with a single trapped Yb^+ using a 369 nm photon bus. The lifetime of the relevant ionic state is longer than that of the ZnO system by a factor of 6, leading to a greatly decreased temporal overlap in their emitted photons and thus decreased fidelity in the final entangled state if left unattended. This temporal mismatch is a long outstanding challenge when entangling disparate quantum systems, and to address it I performed numerical calculations to design an excitation pulse which can shape the emitted In photon to have an overlap of 0.99 with the Yb^+ photon. This leads to a calculated entangled state fidelity of 94% and an entangled state generation rate of 21 kHz

with reasonable experimental parameters.

Future directions of the parabolic mirror project are the construction of an ellipsoidal mirror trap which is expected to collect light from 95% of the solid angle surrounding a trapped ion. This high light collection will enable investigations into the time dynamics of quantum jumps. These jumps occur when a weakly driven system is continuously measured, and their appearance is entirely random. However, recent work in an artificial superconducting atom suggests that there is a latency period in other transitions which precedes a jump, allowing for these events to be 'caught' [1]. We endeavor to confirm this behavior in a trapped ion, confirming the discovery for a real atomic system.

TABLE OF CONTENTS

LIST OF FIGURES

LIST OF TABLES

ACKNOWLEDGMENTS

Boris Blinov has been a phenomenal advisor and a constant source of support throughout my years here, and for that I offer my heartfelt thanks. He was always available to discuss any challenges I may have encountered with my science, and I greatly enjoyed our morning chats when we both arrived to lab early.

I also must thank my reading committee, Steve Sharpe and Deep Gupta, and the remaining members of my supervisory committee, Xiaodong Xu and Munira Khalil. Thank you for your feedback, and your flexibility when the pandemic and associated lab lock-down lead to an unexpected shift in my thesis topic.

Many thanks to my fellow graduate labmates Liudmila Zhukas, Alex Kato, and Sara Branson, as well as all of our undergraduate researchers, especially Ali Hasanzadeh, Elle Bernbaum, and Walker Steere, who worked on projects with me. I also want to explicitly thank Mila and Alex for the lovely years we spent working together in Blinov Lab. Your companionship and support has been invaluable, and I have learned a lot from you.

I have also received extraordinary support from many other members of my graduate student cohort, especially Maria Viitaniemi and Natalie Klco. Maria has been a source of light throughout even the rainiest of Seattle days and the discussions I shared with Natalie always furthered both my understanding of and excitement for quantum mechanics.

Finally, I have to thank my parents Rob and Barb Lilieholm and my brother Tom Lilieholm. You have been unwavering sources of support and encouragement throughout the progress of my degree and my life, and I wouldn't have made it without you.

Chapter 1

INTRODUCTION

Human understanding of the universe underwent a rapid revolution around the start of the 20th century when the field of quantum mechanics was born. It was discovered that the world behaves in a very peculiar manner on the smallest of scales. Quantum particles exist in multiple states at the same time, and may not actually be just particles after all. Pure states are described by the quantum mechanical wave function, which provides the probabilities that a system is found in a certain state when measured. Before measurement, the system may be in all of these states at once, a condition known as superposition.

There is no way to observe the superposition of states. However, measurement collapses the wave function to a single definite value, and repeated measurements of identically created systems can generate statistics which inform as to the original superposition of states. This wave function collapse is thought to occur instantaneously, according to the Copenhagen interpretation of quantum mechanics.

Along with this instantaneous collapse, transitions between different quantum states while the system was being weakly observed and continuously measured were thought to occur instantaneously as well. These instantaneous transitions are known as quantum jumps. As the system is being constantly observed, it does not enter into a superposition state, instead going directly into the new energy level. This continuous measurement also allows for the quantum Zeno effect, where a continuously measured system which is strongly driven fails to transition, as the continuous measurement aborts the superposition states with the other level before it is probabilistic to measure the system at a different energy. Another important facet of these transitions is their unpredictability. Quantum jumps are inherently random, with no way to determine when one will occur. This is

distinct from wavefunction evolution, which follows a set of equations determined by the energy levels involved and the drive power.

The superposition of states allows for quantum entanglement to occur. When two systems are entangled, the measurement of one system provides information on the state of other entangled system as well. For example, suppose there are two entangled systems (A and B), each in an equal superposition of state $|0\rangle$ and $|1\rangle$:

$$|\Psi\rangle = \frac{1}{\sqrt{2}}\left(|0\rangle_A |0\rangle_B + |1\rangle_A |1\rangle_B\right). \tag{1.1}$$

Although both systems start in equal superpositions of $|0\rangle$ and $|1\rangle$, measurement of one system collapses the wavefunction to match.

These peculiar qualities of quantum-scale systems offer some exciting possibilities for future scientific progression. Computer technology has been advancing with the rapidity described by Moore's Law, which is an empirical law stating that the number of transistors on an integrated circuit doubles every two years, for the past several decades. However, this rapid pace of advancement has begun to slow, as quantum effects begin affect the increasingly smaller transistors needed. As this leads to a slowing in the increase of technology, many have begun to wonder what will come next. Quantum computers are a strong candidate for humanity's next great technological leap forward. These devices are able to run massively parallel operations by taking advantage of things such as quantum entanglement and superposition states, leading to devices which can solve in hours problems which previously couldn't be solved within the lifetime of the known universe when run on a classical computer.

Technology isn't yet at the state where quantum computers are available for general purchase on the market, but that doesn't mean there isn't a fierce interest in getting it there. As many research groups, labs, and companies work towards creating these systems, a wide range of candidates emerges. Superconducting qubits allow for rapid gates, but lack long coherence times[6]. Anyons promise tantalizingly low error rates, but are difficult to experimentally actualize[7].

Trapped ions are a promising candidate, as they offer long coherence times, clear options for scaling, and the ability to be paired with other qubit systems, which is one of the experiments

discussed in this text. Ions can act as the qubit, while emitted photons carry information and entanglement to other elements. The parabolic mirror trap described in this thesis is uniquely suited for these tasks as it has a light collection an order of magnitude better than other ion trap designs, allowing for much more rapid entanglement and gates.

Semiconductor donor defects are another strong candidate. Utilizing donor-bound exciton transitions, they perform operations rapidly, though often have lower coherence times than other systems, such as trapped ions. Additionally, the efficiency of photon production varies wildly dependent on the type of semiconductor and donor used.

Hybrid quantum systems offer an opportunity to combine the advantages of some of these different qubit systems together while hopefully avoiding some of the individual qubit downfalls. A hybrid system could, for example, utilize trapped ions for quantum memory and donor defects for gate operations, producing a quantum computer which is faster and more reliable than either qubit could achieve on its own.

In order to construct one of these hybrid systems, there needs to be a way to link these disparate qubits together. For optical systems, like the ones mentioned above, a photon bus can be utilized to entangle these separate systems. However, this requires the ability to collect or generate identical photons from the two systems for efficient entangling operations, which is a nontrivial task.

In this text, I present a scheme to remotely entangle a ZnO donor defect and a Yb^+. The ion is trapped in a novel parabolic mirror trap, whose properties I investigate in chapter 4. The temporal profile of the photon emitted from the ZnO system must be modified to match the Yb^+ photon. In chapter 6, I perform the necessary pulse shaping calculations to demonstrate how this can be done and calculate the sort of performance we can expect from such an entangled state.

Chapter 2

QUANTUM MECHANICS

2.1 Wavefunction

Quantum systems are described by their wavefunction,

$$|\Psi\rangle = \sum_{a'} c_{a'} |a'\rangle \tag{2.1}$$

where the system is in a superposition of all possible states $|a'\rangle$. These states are the eigenfunctions of the system's Hamiltonian for the wavefunction. The probability of the system being found in the state $|a'\rangle$ is given by $|c_{a'}|^2$. When a measurement of an observable of the system is made, it collapses into one of the eigenstates of that observable.

Take, for example, an electron's spin states. Electrons can have spin up ($|\uparrow\rangle$) or spin down ($|\downarrow\rangle$). The wavefunction describing these spin states would then be

$$|\Psi\rangle = \alpha |\uparrow\rangle + \beta |\downarrow\rangle \tag{2.2}$$

where $|\alpha|^2 + |\beta|^2 = 1$ and $|\alpha|^2$ is the probability of measuring the electron in the spin up state. Before measurement, the electron is in a superposition of spin up and spin down, and after it is definitively in the found state.

States whose operators commute with the operator used to make the measurement are unaffected. For example, measuring the position of a particle has no effect on its spin properties because they act on different degrees of freedom in the system. On the other hand, position and momentum are incompatible observables because measuring the position of a particle will change its momentum.

2.1.1 Coherent Evolution

When unobserved, wave functions evolve according to,

$$|\Psi(t)\rangle = e^{\frac{-iHt}{\hbar}} |\Psi(0)\rangle , \tag{2.3}$$

where H is the Hamiltonian describing the total energy of the system, $\hbar$ is Plank's constant, and $|\Psi(0)\rangle$ is the initial state of the system. In atomic systems, we can use this relation to describe an atom acted upon by a driving force (such as a laser) with energy close to the transition frequency. Solutions to Eq. 2.3 provide equations which describe the atom's transition between different energy levels. Measurement then collapses the atom's state into one of the described energy levels with probabilities described by the rate equations (discussed more in Sec. 3.2).

2.1.2 Quantum Jumps

A system that is weakly driven and continuously measured will undergo quantum jumps (Fig. 2.1). These are transitions that occur apparently instantaneously, without any evolution of the wave function because the constant measurement keeps collapsing the wavefunction. The occurrence of these jumps is random and cannot be predicted by Schrodinger's Equation, and the time scale of these transitions was thought to be instantaneous for decades.

The existence of quantum jumps was first proposed in 1913 by Niels Bohr[8], though they were not widely accepted by the scientific community until they were observed in a trapped barium ion by Hans Dehmelt in 1986[9]. Quantum jumps in a trapped ion can be detected as abrupt changes in photon count rate as the ion jumps to or from a long-lived dark state (Fig. 2.2).

Recent work by Minev *et al.*[1] has revealed that these transitions are not as instantaneous or unpredictable as previously thought. Instead, there is a latency period before the jump occurs where the fluorescence count rate drops to zero but the system has not yet jumped to the dark state. This latency period can be used to determine when a jump is about to occur. Additionally, jumps were found to have some sort of dynamic nature, as it was shown that detected jumps could be 'caught and reversed.' In Chapter 7, I discuss our plan to investigate this behavior in a trapped barium ion.

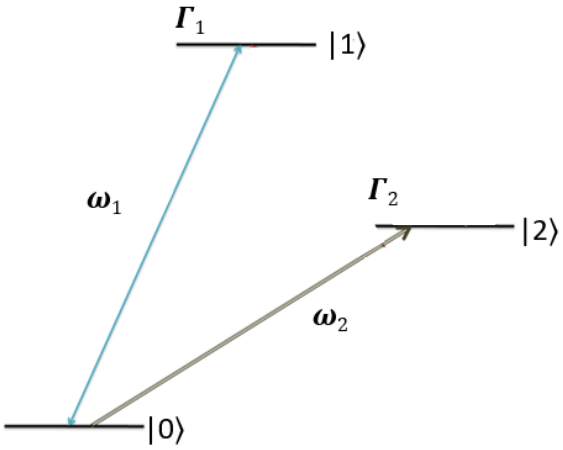

Figure 2.1: Sample energy levels of an ion undergoing quantum jumps. The $|0\rangle \longrightarrow |1\rangle$ transition is strongly driven and continuously monitored while the $|0\rangle \longrightarrow |2\rangle$ is weakly driven. Quantum jumps occur between $|0\rangle$ and $|2\rangle$.

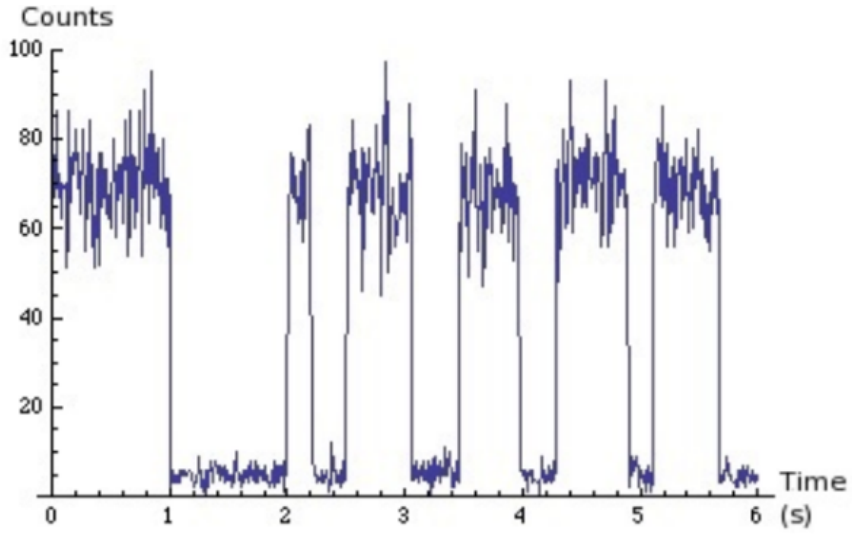

Figure 2.2: Fluorescence signal shown as the photon count rate coming from the ion undergoing quantum jumps is plotted versus time. A quantum jump has occurred when the fluorescence count rate abruptly changes, indicating that the ion has jumped to or from a long-lived 'dark' state. *Image credit: Nathan Kurz[2]*

2.2 Entanglement

Systems consisting of multiple particles can be described by a single wavefunction. For example, a system consisting of two particles (labelled 1 and 2) with single particle possible states $|0\rangle$ and $|1\rangle$ can be written as:

$$|\Psi\rangle = (A|0\rangle + B|1\rangle)_1 + (C|0\rangle + D|1\rangle)_2 \tag{2.4}$$

and shortened to:

$$|\Psi\rangle = AC|00\rangle + AD|01\rangle + BC|10\rangle + BD|11\rangle \tag{2.5}$$

where the states have been multiplied out and particle identity is determined by order in the ket instead of a subscript, with the first entry being particle 1 and the second particle 2.

This wavefuction can still be separated out into separate wavefunctions for the two component particles. When the wavefunciton cannot be separated, the particles are entangled. For example, a two-particle quantum state given by

$$|\Psi\rangle = \frac{1}{\sqrt{2}}|00\rangle + \frac{1}{\sqrt{2}}|11\rangle \tag{2.6}$$

is a maximally entangled state since measurement of one particle definitively informs on the state of the other.

For quantum computing purposes, it is often desirable to entangle two systems which are a distance apart. This allows for the construction of larger entangled systems, or entangled systems built of different types of qubits. A common way of approaching this is through the use of a photon bus. Photons are useful for conveying quantum information because they are easier to manipulate than other quantum systems and move quickly.

One approach to remotely entangling two distant systems is through the creation of a single photon of unknown provenance. This scheme was proposed by Cabrillo *et al.* in 1999 [10]. As described in that work, two systems are excited with weak excitation probability (<10%) and a detector is placed exactly in the middle of the two systems. Detection of a single photon indicates that one system has undergone its excitation cycle while the other has not (assuming no losses).

The state of one system is then entangled with the other, giving an entangled state of

$$|\Psi\rangle = \frac{1}{\sqrt{2}}(|10\rangle + |01\rangle) \tag{2.7}$$

where $|0\rangle$ indicates the system has not undergone the transition and $|1\rangle$ indicates that it has. The first value in the ket represents one system; the second value the other. Observing one of the two systems collapses the superposition, as we know what state the other must be in.

Of course, there are further considerations which arise when trying to replicate this experiment in the lab. Phase differences arising from the excitation laser phase or path length differences give distinguishability to the photons, damaging the fidelity of the final state. It is also difficult to position a detector so that it gets no clue as to the origin of a photon when they approach through free space, so fiber coupling and a beamsplitter are often used.

Fidelity is a way to measure how similar a state is to a desired state, and is calculated through:

$$F = \langle \Psi_{ent} | \rho | \Psi_{ent} \rangle , \tag{2.8}$$

where ρ is the density matrix of the system being tested and $|\Psi_{ent}\rangle$ is the desired state. Fidelity can be used to compare how close an experimentally created state is to a maximally entangled state providing a way to quantify the success of entanglement generation experiments.

Chapter 3

ATOMIC PHYSICS

3.1 Atomic Structure

Atoms consist of a positively charged nucleus containing at least one proton and at least one electron orbiting around it. This motion is quantized according to the principles of quantum mechanics. The simplest case is that of the hydrogen atom, which consists of a single proton and electron. It can be solved precisely, and other atomic systems with single valence electrons are treated as perturbations of the hydrogen system.

To determine the hydrogen wavefunctions, we need to start with the Hamiltonian. As described in Sec. 2.1.1, the Hamiltonian is a description of the total energy in a system. For the case of a single electron orbiting a proton,

$$H = \frac{\hat{p^2}}{2m_e} + V(r) \tag{3.1}$$

where m_e is the electron mass, $\hat{p}$ is the momentum operator, and $V(r)$ the potential energy. In this case, the potential energy is given by the Coulomb potential between the electron and proton,

$$V(r) = \frac{-e^2}{4\pi\varepsilon_0 r}. \tag{3.2}$$

where ε_0 is the permittivity of free space and e is the electron charge.

The momentum operator $\hat{p}$ can also be written as $-i\hbar\nabla$. This leads to the time independent Schrodinger equation,

$$-\frac{\hbar^2}{2m}\nabla^2\Psi + V\Psi = E\Psi. \tag{3.3}$$

Converting to spherical polar coordinates this expression becomes

$$\frac{1}{R(r)}\frac{\partial}{\partial r}\left(r^2\frac{\partial R(r)}{\partial r}\right) - \frac{2m_e r^2}{\hbar^2}[V(r)-E] = \frac{-1}{Y(\theta,\phi)}\left[\frac{1}{sin\theta}\frac{\partial}{\partial\theta}\left(sin\theta\frac{\partial}{\partial\theta}\right) + \frac{1}{sin^2\theta}\frac{\partial^2}{\partial\phi^2}\right]Y(\theta,\phi) \tag{3.4}$$

where we are seeking a solution of the form $\Psi = R(r)Y(\theta,\phi)$. This substitution allowed for the creation of the separable equation above.

Solutions to the angular wavefunctions are

$$Y_{l,m}(\theta,\phi) = \sqrt{\frac{(2l+1)}{4\pi}\frac{(l-m)!}{(l+m)!}}P_l^m(cos\theta)e^{im\phi} \tag{3.5}$$

where l is the orbital angular momentum quantum number, m is the magnetic quantum number, and $P_l^m(x)$ are the associated Legendre polynomials. These solutions are known as the orbital angular momentum eigenfunctions, and each solution with its combination quantum numbers l, m corresponds to a different state the hydrogen atom can be in.

The radial wavefunction solutions are

$$R_{n,l}(r) = \left(\frac{2}{na_0}\right)^{\frac{3}{2}}\sqrt{\frac{(n-l-1)!}{2n[(n+l)!]^3}}e^{\frac{-r}{na_0}}\left(\frac{2r}{na_0}\right)^l L_{n-l-1}^{2l+1}\left(\frac{2r}{na_0}\right) \tag{3.6}$$

where l is the same orbital angular momentum quantum number as in the angular solution, n is principle quantum number, a_0 is the Bohr radius (0.529×10^{-10} m), and $L_{n-l-1}^{2l+1}(x)$ is the associated Laguerre polynomial. The approximate wavefunction for hydrogenic ions (one electron orbiting a nucleus with Z protons) can be found by substituting $r \longrightarrow Zr$.

The energies of these various states are

$$E = -\frac{m_e}{2\hbar^2}\left(\frac{e^2}{4\pi\varepsilon_0}\right)^2\frac{1}{n^2}. \tag{3.7}$$

with the ground state energy of -13.6 eV occurring at n=1, where l=0 and m=0.

3.1.1 Zeeman Effect

The energy levels described in Eq. 3.7 represent the unperturbed energy levels. In reality, there are many effects and interactions which split and shift these levels. One such interaction is the Zeeman effect, which occurs when an atom is in an external magnetic field. The Hamiltonian for this interaction is

$$H = g_F\mu_B\mathbf{F}\cdot\mathbf{B}. \tag{3.8}$$

where $\mathbf{F} = \mathbf{J} + \mathbf{I}$, the sum of the atom's total angular momentum $\mathbf{J}$ and nuclear spin $\mathbf{I}$. It additionally depends upon the external applied magnetic field ($\mathbf{B}$), the Bohr magneton (μ_B), and Lande g-factor g_F. In first-order degenerate perturbation theory, increasing the external magnetic field proportionally increases the spacing of energy levels according to

$$E = g_F \mu_B B M_F. \tag{3.9}$$

where M_F is the projection of $\mathbf{F}$ onto the magnetic field.

This is a powerful tool in atomic physics, as it allows for fine-tuning of transitions between certain atomic energy levels. A specific application is discussed in Chapter 6 where the transitions of a ZnO In donor defect and a Yb ion are tuned to match in order to generate photons with matching frequencies.

3.2 Transitions

Transitions between different energy levels can be driven through application of radiation resonant with the energy difference. This process can be clearly laid out through the example of a two-level atom, leading to the rate equations which describe the changing populations of the two levels.

Starting with the time dependent Schrodinger equation in the form

$$i\hbar \frac{\partial \Psi}{\partial t} = H\Psi \tag{3.10}$$

we can split the Hamiltonian into two parts,

$$H = H_0 + H_1(t) \tag{3.11}$$

where H_0 is the unperturbed Hamiltonian for the standard energy levels as found above and $H_1(t)$ describes the perturbation by an oscillating field (such as a laser) interacting with the atom. $H_1(t)$ perturbs the eigenvalues found earlier for H_0 alone.

The wavefunction for the original Hamiltonian can be written as

$$\Psi_n(\mathbf{r},t) = \psi_n(\mathbf{r}) e^{\frac{-iE_n t}{\hbar}}. \tag{3.12}$$

where $\mathbf{r}$ is a vector describing position as a function of r, θ, and ϕ, E_n is the energy of the n$^{\text{th}}$ energy level, and $\hbar$ is Planck's constant.

As mentioned above, we are imagining a two level system, so

$$H_0\psi_1(\mathbf{r}) = E_1\psi_1(\mathbf{r}) \tag{3.13}$$

$$H_0\psi_2(\mathbf{r}) = E_2\psi_2(\mathbf{r}) \tag{3.14}$$

for our system with levels $|1\rangle$ and $|2\rangle$. Associated with these levels are wavefunctions Ψ_1 and Ψ_2 as well as energies E_1 and E_2.

These lead to the general state of the system described by the following wavefunction:

$$\Psi(\mathbf{r},t) = c_1(t)\psi_1(\mathbf{r})e^{\frac{-iE_1t}{\hbar}} + c_2(t)\psi_2(\mathbf{r})e^{\frac{-iE_2t}{\hbar}}. \tag{3.15}$$

This expression can be rewritten into the more concise form

$$\Psi(\mathbf{r},t) = c_1\,|1\rangle\, e^{-i\omega_1 t} + c_2\,|2\rangle\, e^{-i\omega_2 t} \tag{3.16}$$

where $|c_1|^2 + |c_2|^2 = 1$ and we have taken the simplifications $\Psi_n(\mathbf{r}) = |n\rangle$ and $E_n/\hbar = \omega_n$.

Now suppose the atom is exposed to an oscillating electric field of the form

$$\mathbf{E} = \mathbf{E}_0 cos(\omega t). \tag{3.17}$$

where E_0 is the amplitude of the electric field and ω its frequency. In the dipole approximation, where the extent of the atom is much less than the wavelength of the field, this leads to the interaction Hamiltonian

$$H_1(t) = e\mathbf{r}\cdot\mathbf{E}_0 cos(\omega t), \tag{3.18}$$

which is the energy of an electric dipole. In this case, the dipole is caused by the position of an electron in the oscillating electric field, and the electron position is determined from the wavefunction. In this example, there are two wavefunctions, corresponding to levels $|1\rangle$ and $|2\rangle$. $H_1(t)$ describes the interaction which mixes the two states.

Utilizing the rotating wave approximation and solving the time-dependent Schrodinger equation for this situation, we find

$$|c_2(t)|^2 = \frac{\Omega^2}{W^2} sin^2\left(\frac{Wt}{2}\right) \tag{3.19}$$

where we have used the initial condition $c_1(0) = 1$, $c_2(0) = 0$ and $W^2 = \Omega^2 + (\omega - \omega_0)^2$. Ω is the Rabi frequency, defined as

$$\Omega = \frac{\langle 1 | e\mathbf{r} \cdot \mathbf{E}_0 | 2 \rangle}{\hbar}, \tag{3.20}$$

and ω the oscillation frequency of the applied field while $\omega_0 = (E_2 - E_1)/\hbar$. When the applied field is resonant with the transition ($\omega = \omega_0$), the expression simplifies to

$$|c_2(t)|^2 = sin^2\left(\frac{\Omega t}{2}\right). \tag{3.21}$$

where is is clear to see that the state populations will oscillate between the two energy levels (recall $|c_1|^2 + |c_2|^2 = 1$) at the Rabi frequency Ω.

As seen in Eq. 3.20, this frequency depends on the amplitude of the electric field and the transition being driven. As such, we can used Rabi pulses to drive atomic systems to desired states. Two common cases used are those of a π pulse and a $\pi/2$ pulse. These occur when a laser is applied to an atomic system for duration $t_\pi = \pi/\Omega$ or $t_{\pi/2} = \pi/2\Omega$. A π pulse will invert the populations of the two atomic levels, while a $\pi/2$ pulse will take the system halfway to inversion. For example, if initially in $|1\rangle$, a $\pi/2$ pulse will leave the system in an equal superposition of $|1\rangle$ and $|2\rangle$ (assuming resonant light). These pulses would be used in the work described in Chapter 7.

3.3 Ion trapping

Ions are charged particles; thus their motion can be efficiently controlled by applying electric (and magnetic) fields. From Earnshaw's theorem [11], it is clear that it is impossible to have a stable minimum in a constant electric field, so ions cannot be contained by a constant electric field. There are two common ion trap design which get around this restriction. The first is the Penning trap, which uses a combination of magnetic fields and a static hyperbolic electric field. The other type is a Paul trap, which uses a time-dependent electric field and is the type of trap used in this body of work.

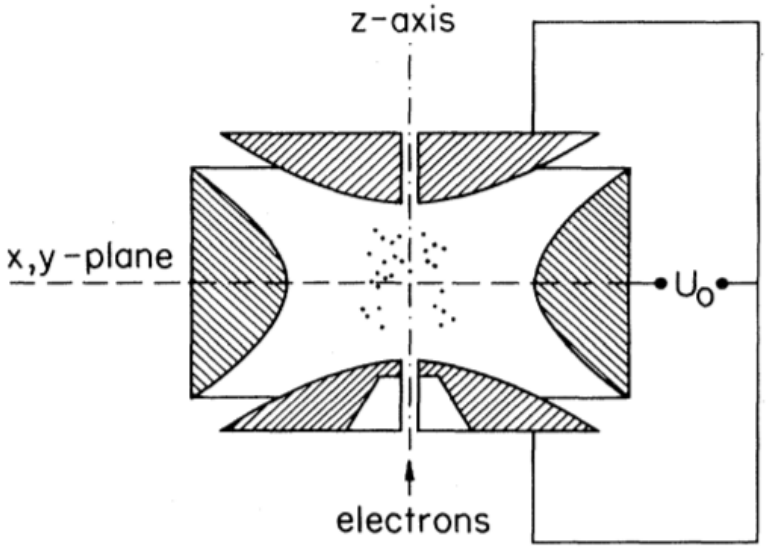

Figure 3.1: Schematic of original Paul trap design. Two hyperbolic electrodes on top and bottom have a constant potential applied to them, while the hyperbolic ring electrode acts as an RF electrode. *Image Credit: Wolfgang Paul [3]*

The original ion trap was designed by Wolfgang Paul and consisted of a hyperbolic ring electrode with an applied radio frequency (RF) voltage and two hyperbolic endcaps of constant potential[3]. The time averaged potential (psuedopotential) has a minimum, which the ions become caught in. Since its conception, this design has undergone a bounty of modifications to produce a fleet of ion trap designs, each with their own specialized advantages. Linear traps [12] consist of four rods and can trap linear chains of ions, which can then be individually addressed and easily entangled with their neighbors through motional mode coupling. Semiconductor chip traps and surface traps [13] allow for individual shuttling of ions across a surface and offer options for scaling ion trap systems. Two-dimensional traps [14] allow for large ion crystals to be trapped and studied. The trap utilized in this body of work is a parabolic mirror ion trap (Chapter 4), which has been designed to optimize light collection from a single trapped ion. Advantages of such a system are increased entanglement generation rates due to greater collection of entangled photons (Chapter 6), and higher time resolution of atomic transitions (Chapter 7).

3.3.1 Ion Confinement

As mentioned above, ions are held in Paul traps through a combination of static and RF electrical fields that create a time-averaged harmonic potential of the form

$$\Phi(x,y,z) = (U + V cos(\Omega t))(x^2 + y^2 - 2z^2) \tag{3.22}$$

Where U is the amplitude of the electric potential applied by the static field, V corresponds to the amplitude of the oscillating electric field, which is applied at RF frequency Ω. The equation of motion for a trapped ion can be found by solving

$$F = -e\nabla\Phi(x,y,z). \tag{3.23}$$

Solving this in one direction, we find

$$x(t) = [x_0 + x_1 cos(\omega_x t)][1 - \frac{2eV}{mR_0^2} cos(\Omega t)] \tag{3.24}$$

where x_0 is the ion's displacement from the center of the trap due to constant voltage offsets, x_1 is the maximum amplitude of the ion's oscillation in the RF psuedopotential well, R_0 emerges from the trap geometry representing the distance from the trap center to the RF electrode (in x direction), Ω is the RF driving frequency, and

$$\omega_x = \frac{1}{R_0}\sqrt{\frac{e}{m}\left(2U - \frac{V}{2}\right)} \tag{3.25}$$

is the secular frequency of the trap in $\hat{x}$ for an ion of mass m.

3.3.2 Ion Cooling

To successfully trap an ion, they must be present in the system. There are several methods for generating ions in vacuum, but in this body of work we used oven tubes containing samples of the atomic element which were ionized by lasers after they emerged of the heated oven tube (see Chapter 5 for more oven details). Ions that emerge from the oven are very hot, in the realm of hundreds of Kelvin. To trap the ions in stable crystals, they need to be cooled down. Doppler cooling[15] is a process which can rapidly bring hot ions down to miliKelvin temperatures.

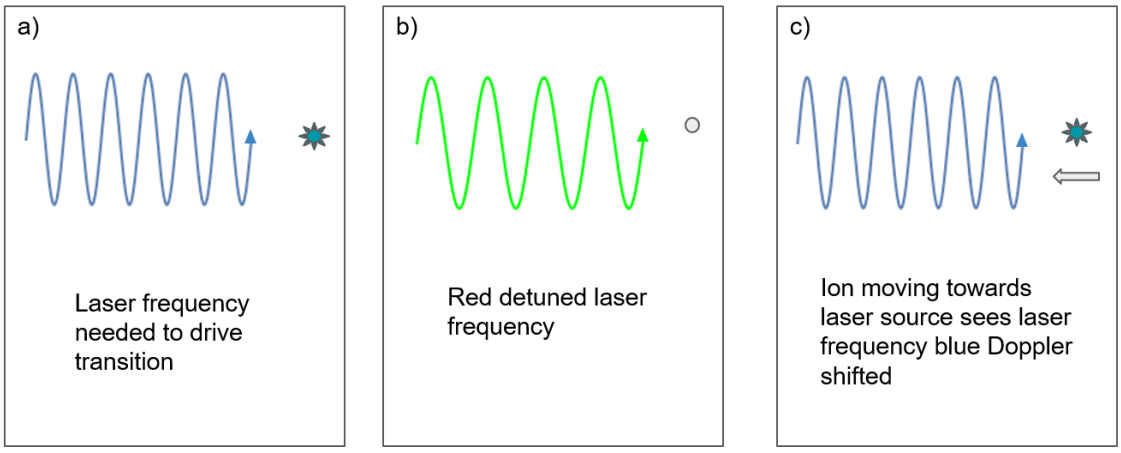

Figure 3.2: a) A trapped ion interacts with a laser resonant with the ion's transition frequency. b) Red detuning the laser makes the stationary ion no longer interact with the laser. c) An ion moving towards the red detuned beam sees the light blue Doppler shifted to the resonant frequency and begins undergoing transitions again.

When an ion interacts with a laser and absorbs a photon, it also gains some momentum in the direction the photon was travelling. When that photon is re-emitted, it emerges in a random direction, imparting a random momentum kick to the ion. The net effect is that the ion will gain momentum in the direction the laser is travelling. By red-detuning the laser, it can be assured that the ion will only absorb a photon when it is moving towards the laser, as it will perceive the light to the blue-shifted to the resonant frequency. Thus, it gains momentum in the direction opposite its momentum and slows slightly. Eventually, the trapped ion will reach the Doppler cooling limit,

$$k_B T = \hbar\Gamma/2 \tag{3.26}$$

where k_B is Boltzmann's constant, T is the ion temperature, and Γ is the linewidth of the cooling transition. While Doppler cooling can greatly reduce the temperature of a hot ion, it alone cannot bring it down to the ground state energy in the harmonic potential generated by the trapping psuedopotential.

Doppler cooling only works in the axis the cooling beam is oriented along. Therefore, to fully cool a trapped ion the cooling laser must have a significant $\vec{k}$ component along each of the three

orthogonal axes of the trap.

3.3.3 Ions as Qubits

The electronic states of trapped ions serve well as qubits. There are two main ways to make a qubit out of the electronic levels in a trapped ion. One is to use two groundstate hyperfine energy levels, forming a hyperfine qubit. Theses qubits are long-lived and phase and frequency stable. The other common ionic qubit is between a ground and an excited state, known as an optical qubit. These duration of these states depends on the lifetime of the excited state used, but are they are long-lived when compared to logic gate times.

Other advantages of trapped ion qubits are their scaling capabilities. Ions held within the same trap are linked by their collective motion in the harmonic trapping potential. This motion is quantized into the harmonic oscillator energy levels, and these levels can be used to aid with atomic gate operations, though they don't serve well as quits on their own because of their sensitivity to external factors, such as ions heating from interactions with lasers. For most operations involving these levels, the ions must be cooled to the Lamb-Dicke regime, $k_B T << \hbar\omega_z$, where k_B is Boltzmann's constant, T is the temperature of the ions, and ω_z is the frequency of the trapping potential in the direction of the oscillations of interest. In the Lamb-Dicke regime, harmonic oscillator energy transitions are limited to ± 1 motional level at a time.

Another way to generate larger systems of entangled ions is to link the ions in separate traps together. Photon mediated entanglement is one way to do this, where the ion emits an entangled photon which can be used to link the ion with another trapped ion. Chapter 6 discusses one way to link two dissimilar systems, one of which is a trapped ion, together via a photonic link.

Barium Ion Qubits

Barium ions are a popular choice for trapped ion quantum computing because barium is hydrogenic when singly ionized and has transitions in the visible or infrared regime. In particular, $^{138}Ba^{+}$ is used for experiments in this work because in addition to the aforementioned advantages this isotope

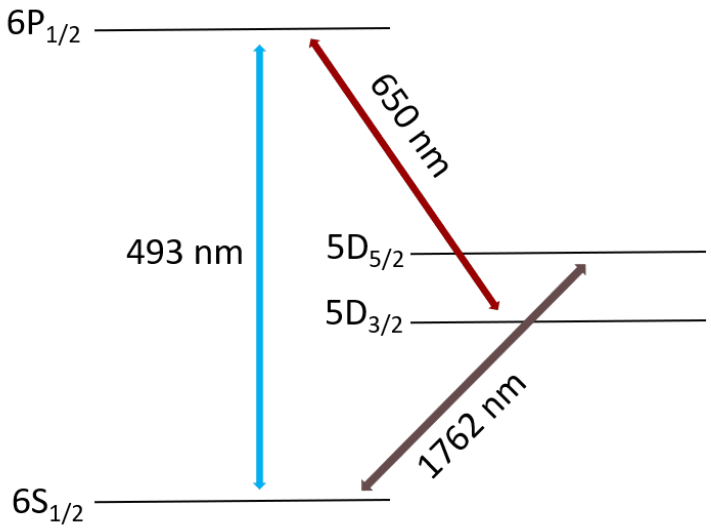

Figure 3.3: Selected levels of $^{138}Ba^{+}$.

has no nuclear spin, which simplifies the level structure.

In our system, a 493 bandpass filter is in place on the optical pathway to limit our collection to only photons from the $6P_{1/2}$ excited state to ground, $6S_{1/2}$. The excited state could also decay to the metastable $5D_{3/2}$ level (24.4% probability). Repumping from this state is attained with a 650 nm laser; else, the state has a lifetime of 80 ns. This allows us to hunt for faint ion signals on our PMT fluorescence counts/second signal by toggling the 650 nm laser on and off. If an ion is trapped, it is eventually pumped to the metastable state and no longer emits 493 nm photons, leading to a drop in collected signal. These levels are also used for Doppler cooling the trapped ion, where their Doppler cooling limit is 3 mK.

Chapter 4

PARABOLIC MIRROR ION TRAP

4.1 Parabolic mirror design

As mentioned in Sec. 3.3, the initial Paul trap design consisted of a ring electrode with an applied radio frequency (RF) voltage and two hyperbolic endcaps of constant potential. The parabolic mirror ion trap is a deformation of the standard Paul trap, where the role of the ring electrode is taken by a parabolic mirror while the hyperbolic endcaps are replaced by a grounded needle emerging from the center of the mirror and a ring electrode over the opening (Fig. 4.1). The ring over the trap opening allows for an uninterrupted path from the ion to the imaging system for better light collection, while the parabolic mirror aids in light collection by reflecting and collimating light emitted from an ion placed at the mirror's surface. The parabolic mirror covers 2π (50%) of the solid angle surrounding the trapped ion, and the shape of the surface is described by

$$z(\rho, f) = \frac{\rho^2}{4f} - f \tag{4.1}$$

where $f = 2$ mm and ρ is the distance from the z axis to the mirror surface.

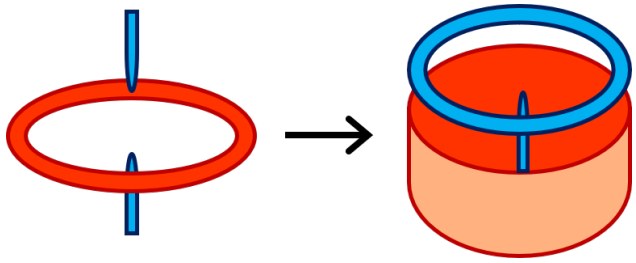

Figure 4.1: Left: Schematic of a traditional Paul trap. Right: Parabolic mirror ion trap schematic. In both images, red serves as the RF electrode and blue for the grounded endcaps. *Image credit: Carolyn Auchter*

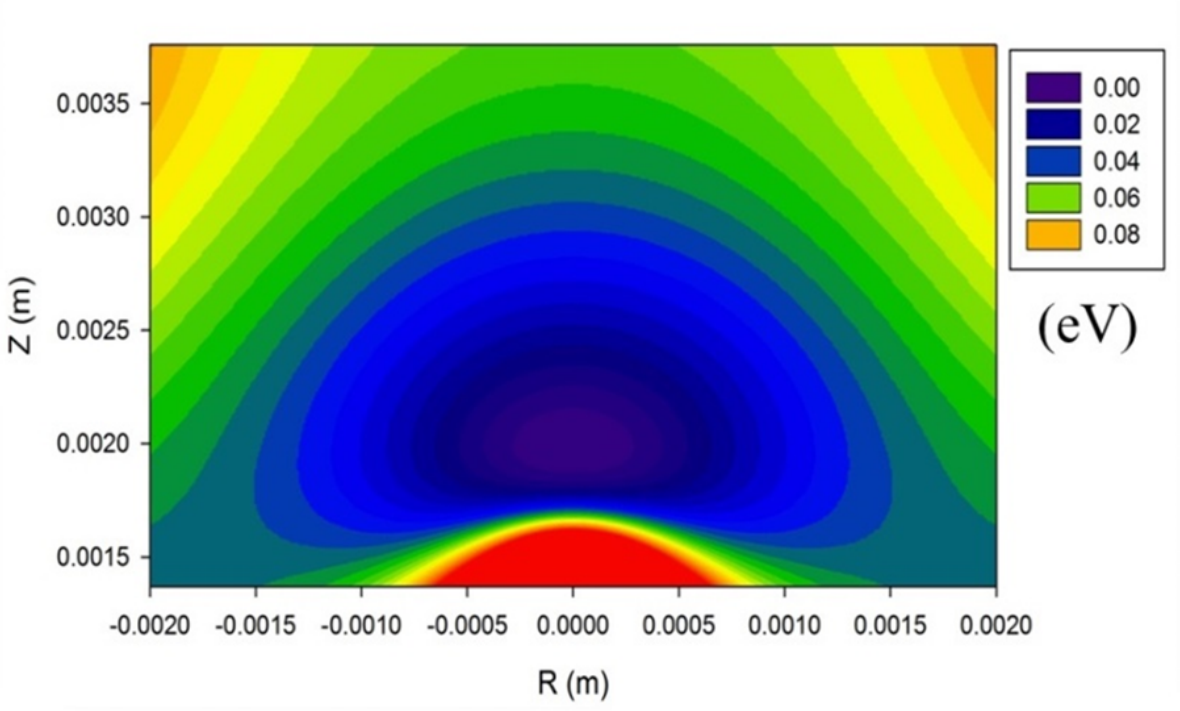

Figure 4.2: Psuedopotential plot of the parabolic mirror trap. The parabolic mirror serves as the RF electrode and has its vertex located at the origin. The grounded needle electrode is centered radially and emerges from the bottom of the plot (z=0). The field changes rapidly off the needle's sharp point, and the ion becomes trapped in the minimum of the potential (purple region of plot). *Image credit: C.K. Chou*

This trap is an evolution of our lab's previous spherical mirror trap design [16]. The advantages of using a parabolic mirror instead of a spherical mirror lie in the parabolic mirror's ability to collimate light from a source placed at its focus, leading to greater light collection and improved image quality [17]. In 2007, Leuchs proposed a design for using a parabolic mirror to enhance light collection [18], and actualized it in 2012 [19]. Their design involved placing a mirror around the entire trapping apparatus to catch light leaving the ion in directions other than the camera. However, since the mirror was incorporated outside the trapping apparatus, some of the photons were blocked before they could reach the mirror. Our design which uses the mirror as the RF electrode is able to avoid this problem as there is nothing between the ion and the reflecting surface.

The psuedopotential of the parabolic mirror trap is stronger in the axial direction than radial,

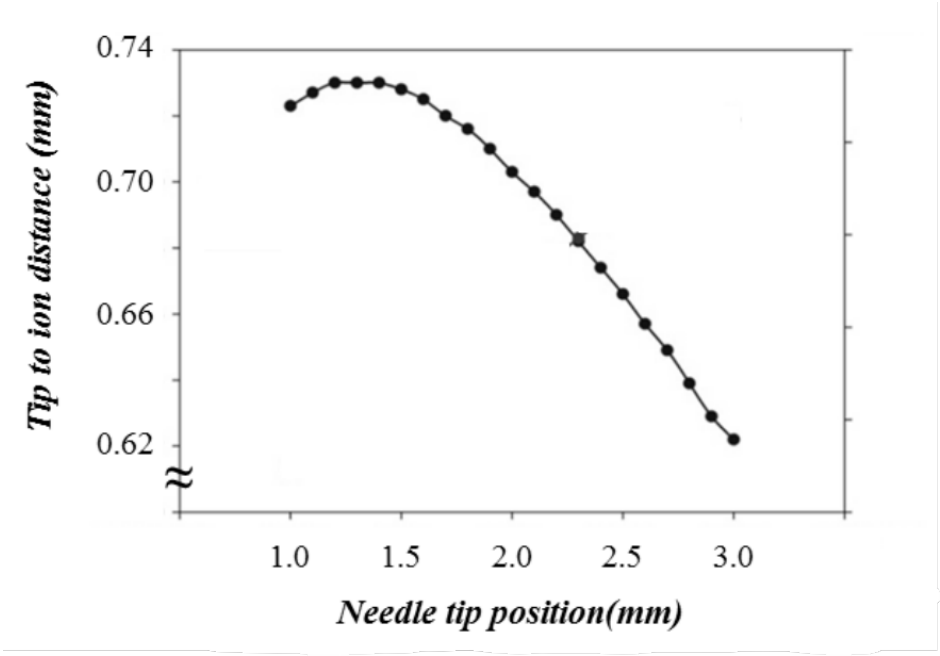

Figure 4.3: Simulation of the distance between the needle tip and the location of a trapped ion as the needle is pushed further from the vertex of the parabola. The ion is in focus when the needle is placed approximately 1.3 mm above the vertex. *Image credit: C.K. Chou*

creating a minimum where the ion becomes trapped (Fig. 4.2). For 1 W of RF power, the trapping depth is approximately 0.03 eV. The location of the psuedopotential minimum is very sensitive to the position of the needle, as its sharp point generates a rapid change in the electric field. The minimum of the psuedopoential is located about 0.7 mm above the tip of the needle, thus by moving the needle we can shift the location of the trapped ion (Fig. 4.3). The needle is attached to a linear actuator which allows for axial placement of the ion. As mentioned above, to properly utilize the parabolic mirror, a trapped ion must be located at its focus. However, in the original iteration of the parabolic mirror trap the ion cannot be trapped at the focus of the mirror. The barium source (Sec. 5) is oriented to send a spray of atomic barium across the opening of the trap, not into the focus. This was done to prevent a buildup of barium from forming on the surface of the mirror, leading to a degradation in image quality and unpredictable trapping location due to stray fields from the barium deposit.

4.2 Construction

The trap is built of a parabolic mirror with an applied RF potential, bias plates to relocate the ion radially, a grounding plate to constrain the ion axially, a grounded needle to confine the ion in the other axial direction, and a linear actuator to move the needle and thus the ion. The mirror is single-point diamond turned out of high purity aluminum to ensure high reflectivity. The shape of the mirror is very close to an ideal parabola near the vertex of the mirror (deviation < 50 nm), while away from the vertex it may deviate from the desired parabolic shape by as much as 1 μm, according to the manufacturer. Fig. 4.4 shows the SolidWorks schematic for the trap apparatus. Assembling the trap structure is a nontrivial process, as care must be taken to electrically isolate the various components. In particular, the parabolic mirror serves as the RF source and thus cannot have contact with any other trap components, including screws which connect to the base plate.

The parabolic mirror is mounted on eight alumina pins which are set into the base plate, and an alumina isolation ring keeps the mirror from sliding back into contact with the base plate (Fig. 4.5A). The alumina pins terminate in contact with the upper grounded electrode. A series of springs and spacers (Fig. 4.5B) provide tension which secures the mirror.

This spring pressure leads to difficulty when assembling the apparatus, as the series of spacers, springs, and electrodes are longer than the length of the alumina pins when the springs are uncompressed. To successfully construct the apparatus, I found that the bias plates had to be tied down with thin wires to compress the springs and allow the final components to be placed. Once the top grounded plate was secured, the wires were cut and removed from the trap.

Standard vacuum hardware such as an ion pump, ion gauge, and titanium sublimation pump (Ti Sub) are used to keep the system under ultra-high vacuum ($\sim 10^{-10}$ torr) and monitor it for pressure changes(Fig. 4.6). The ion pump runs continuously and maintains the system at ultra-high vacuum. The Ti Sub pump is run monthly to remove noble gases which leak into the system that the ion pump is unable to remove. A bakeable valve connects the system to external pumps when it is initially pumping down from atmosphere while baking out. The actuator moves the needle axially, and the ion gauge measures vacuum pressure within the system. The arrangement of the

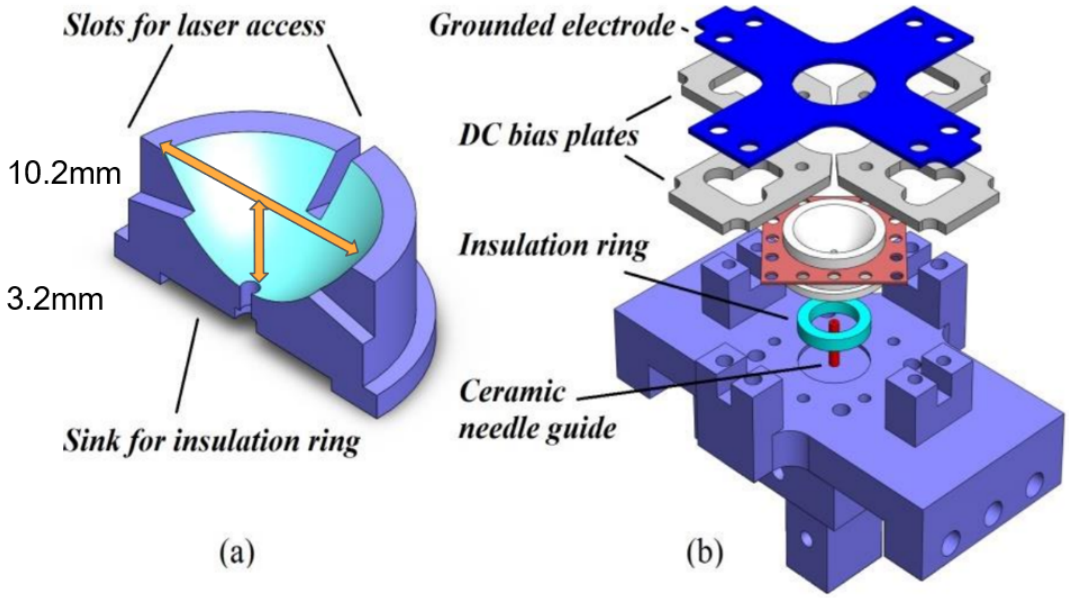

Figure 4.4: SolidWorks schematic of parabolic trap. a) The parabolic mirror which serves as the RF electrode has an opening of 10.2 mm and a depth of 3.2 mm. Four slots around the edges of the mirror allow the laser to access the ion when located axially within the mirror. The focus of the parabola is 2 mm above the vertex. b) Incorporating the parabolic mirror into the trapping apparatus. The mirror needs to be electrically isolated from the other components as it serves as an RF electrode. A cross shaped grounded electrode on top (blue) and grounded needle (through red ceramic needle guide) form the other electrical components of the trap. Four DC bias plates allow for radial positioning of a trapped ion. *Image credit: C.K. Chou*

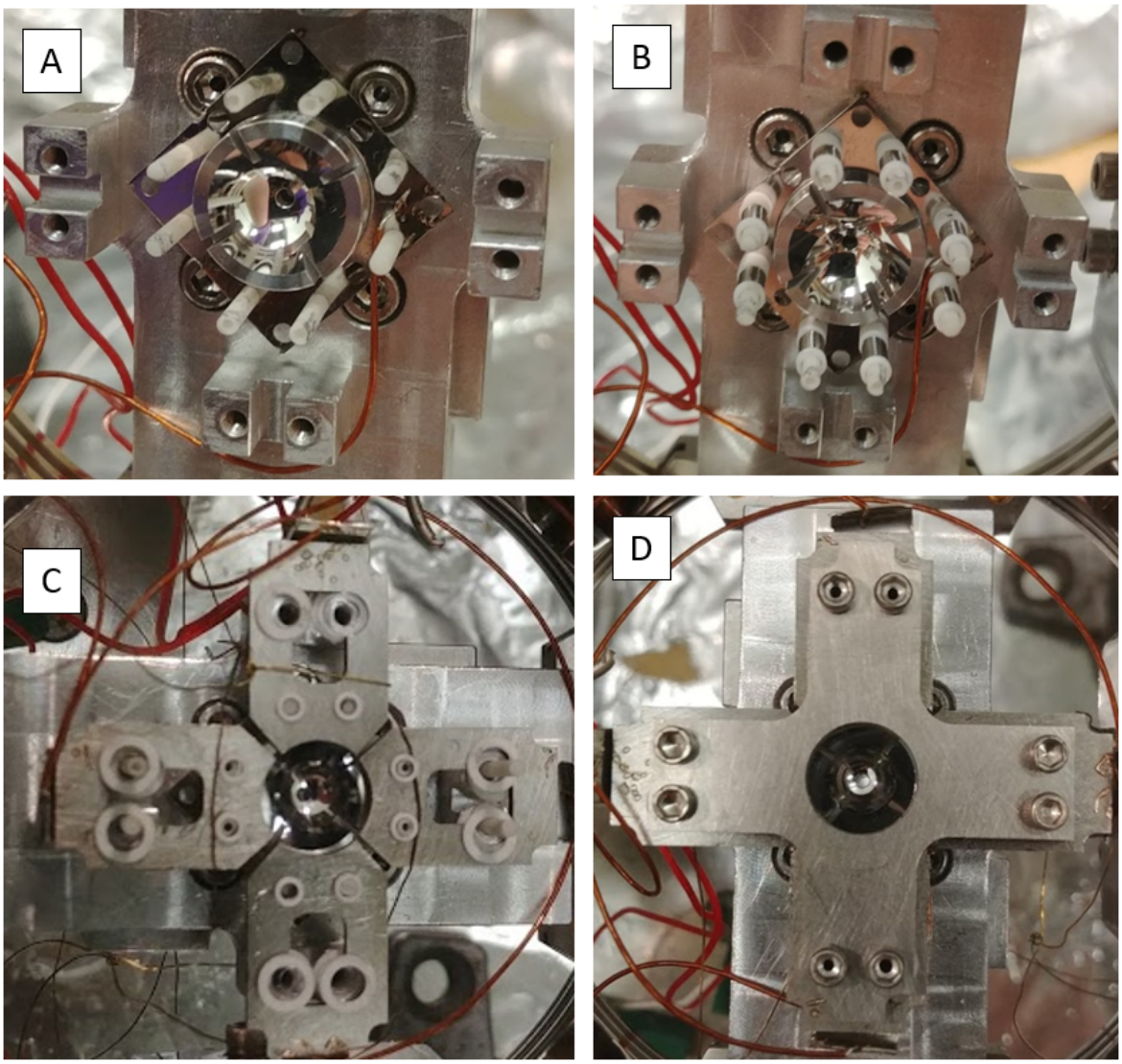

Figure 4.5: Process of assembling parabolic mirror trapping apparatus. A) The mirror must be electrically isolated from the main trap housing. It sits upon an insulating ring (not visible) and is mounted on eight alumina pins. B) Each pin has a spring sandwiched by alumina spacers slid on it. The spring maintains the tension necessary to hold the mirror stationary against the insulating ring. C) Four bias plates are mounted on the alumina pins and the 'ears' of the base trap block. Again, these are electrically isolated from the rest of the apparatus by alumina spacers. D) The grounding plate is secured with screws to the top of the stack through to the base trap block. The screws are isolated from the bias plate by sapphire spacers which sit within the bias plate screw openings.

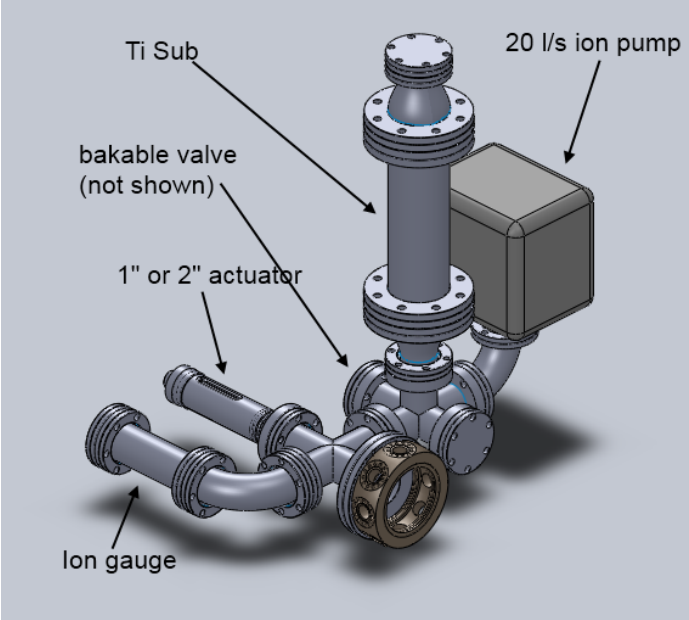

Figure 4.6: Complete vacuum system associated with the parabolic mirror ion trap. *Image credit: C.K. Chou*

various components is constrained by the space limits of the large oven used to bake out the system.

4.3 Characterizing performance of parabolic mirror trap

4.3.1 Light collection

To characterize the light collection efficiency of the parabolic mirror trap, the preceding graduate student, C.K. Chou, performed a single-photon counting experiment. The experiment was performed with $^{138}Ba^{+}$, utilizing its $6P_{1/2}$ excited state and $5D_{3/2}$ metastable state (Fig. 4.7). The ion can be driven to the excited state with a 493 nm laser. From that excited state, the ion can either decay back to the ground state (75.6% chance) or to the metastable state (24.4%) (Fig. 4.8). By optically pumping with a 493 nm laser for 500 ns, the ion can be placed in the metastable excited state with near unit efficiency. From there, a 650 nm laser excited the ion to the excited state, where it will decay to ground (or the metastable state for re-excitation), generating a single 493 nm photon.

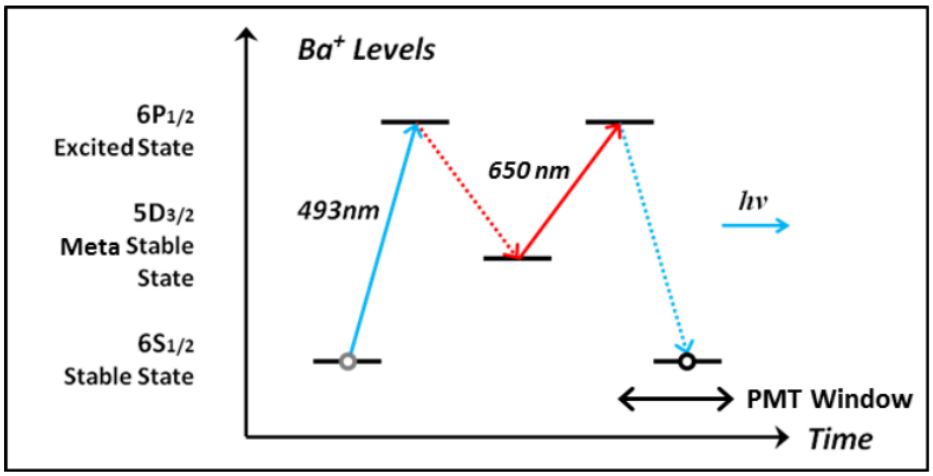

Figure 4.7: Barium excitation scheme used to generate a single photon. The ion was excited by a 493 nm and 650 nm laser along the solid line transitions and spontaneously decayed along the dotted paths. The lifetime of the $6P_{1/2}$ level is short (8 ns) compared to that of the metastable $5D_{3/2}$ state (82 s), allowing the ion to be driven to the metastable state with near 100% efficiency with 500 ns of optical pumping. From the metastable state, excitation with the 650 nm laser allowed the generation of one and only one 493 nm photon, which is detected by a photomultiplier tube (PMT) during the detection window. *Image credit: C.K. Chou*

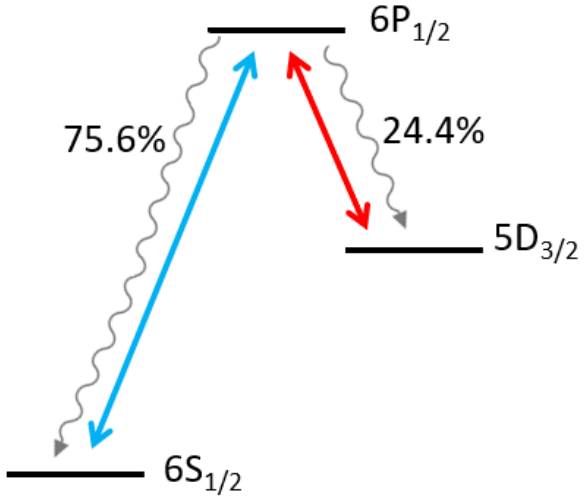

Figure 4.8: Selected barium energy levels with the decay probabilities shown for the excited state $6P_{1/2}$.

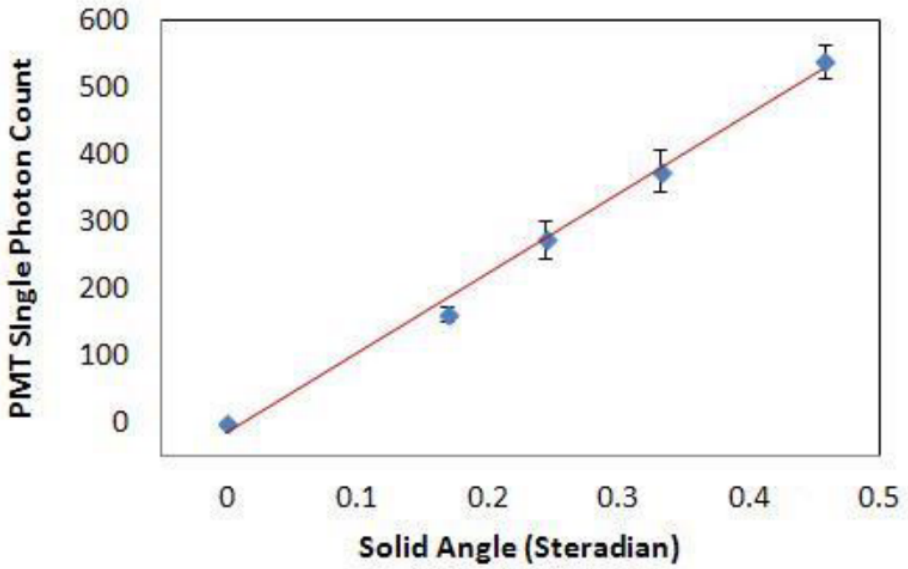

Figure 4.9: Dependence of single photon counting on solid angle through which light is collected. Each data point represents the number of photons collected out of 1 million single photon events at a certain solid angle of light collection. Extrapolating the line to 47,675 photon counts gives a solid angle of 4.9 steradians, equal to approximately 39% of the 4π solid angle. *Image credit: C.K. Chou*

This process was repeated one million times and 47,675 single photons were detected. This results in approximately a 5% efficiency for detecting single photons. This value does not account for photon loss due to reflection and transmission, as well as the PMT quantum efficiency. To determine the mirror's photon collection efficiency, we measured the dependence of single photon count rate on the solid angle through which light was collected. A calibrated iris was integrated into the beam path, and the experiment was repeated at different known solid angles of collection. The parabolic mirror was not utilized during this time. The calibration curve (Fig 4.9) was used to determine that the parabolic mirror was collecting light from 39% of the solid angle surrounding the trapped ion, which was an improvement over the 25% of the lab's spherical mirror trap [16].

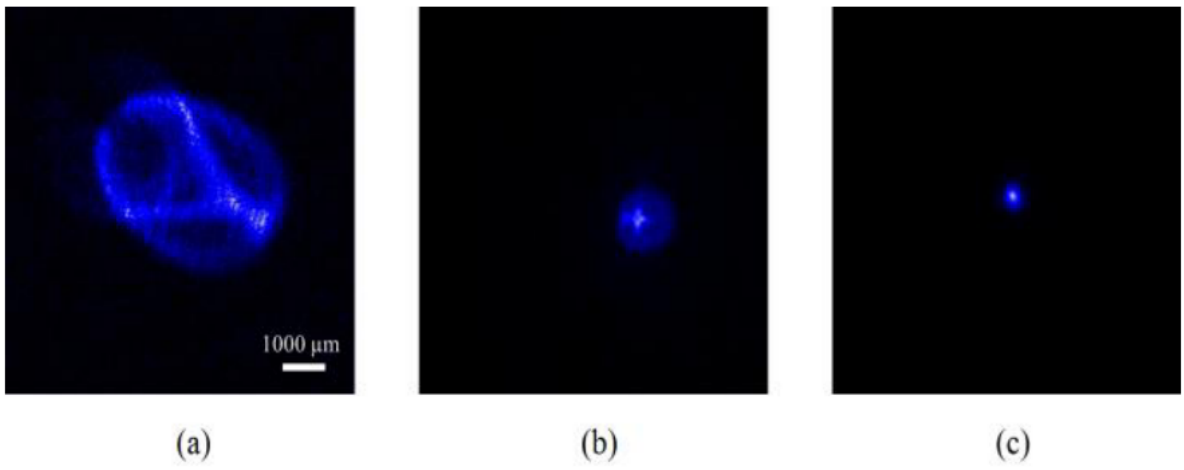

Figure 4.10: A single trapped ion being moved radially to the center of the parabolic mirror. a, b)Offset from the focal location causes a larger image with aberrations from the laser access slots in the parabolic mirror. c) The ion image become cleanest when at the focus of the mirror. *Image credit: C.K. Chou*

4.3.2 Image quality

The upgrade from a spherical mirror ion trap to parabolic had two main goals; improved light collection (discussed above) and improved image quality. To measure the image quality, a spherical lens with a long focal length (1000 mm) was incorporated into the beam path to focus the collimated light reflected from the parabolic mirror. The long focal length ensured that the additional lens did not introduce any additional aberrations. The ion was then placed at the center of the parabolic mirror by adjusting the voltages of the four bias plates (Fig. 4.10).

The ion spot size was defined as $1/e^2$ the peak intensity, and found to be 1065 μm, with a system magnification of 500. This indicated that the optical resolution of a single ion was 2.1 μm. For optimal image quality, we would expect the optical resolution to match the diffraction-limited Airy disc diameter, 1.22 $\times\lambda/NA$, which is $\sim$0.61 μm for our system at 493 nm. Instead, we realized that the image collected was 3.4 times larger than expected.

The ion spot size increases as it moves away from the focus of the mirror. Ray tracing simulations were performed to see how different offsets would affect the point spread function size (Fig.

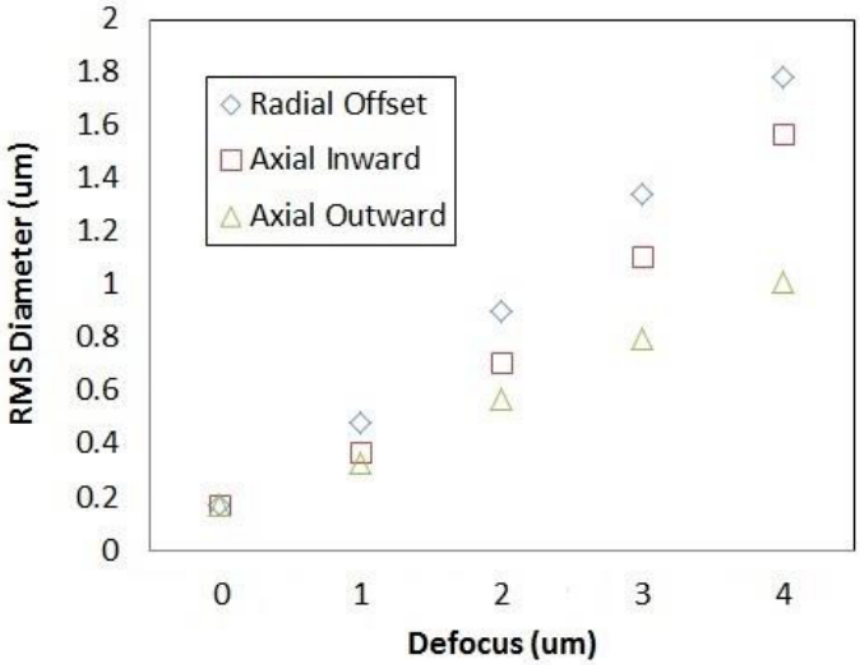

Figure 4.11: Results of ray tracing simulations into the effect of ion defocus on the spot size. The ion image spot size is plotted versus the displacement from the parabolic mirror focus in both the radial and the axial directions. Experimental control over ion position was better than 2 μm. *Image credit: C.K. Chou*

4.11). These simulations revealed that ion positioning was not the sole source of the large spot size. The ion could be placed reliably within 2 μm of the focus with the use of the linear actuator and bias plates, and ray tracing determined that a 2 μm defocus would lead to a spot size of no greater than 1 μm, less than half our measured spot size.

With this avenue satisfied, we set out to determine if the problem was errors in the shape of the parabolic mirror or imperfections in its surface. A Thorlabs DMP40 deformable mirror was utilized for this investigation. The deformable mirror uses 40 individual piezos to deform its surface and correct aberrations in the light emerging from the parabolic mirror (Fig.4.12). The deformable mirror was placed outside the vacuum system but before the 1000 mm focusing lens.

The final corrected image size was 1.7 μm; an improvement over the uncorrected image size

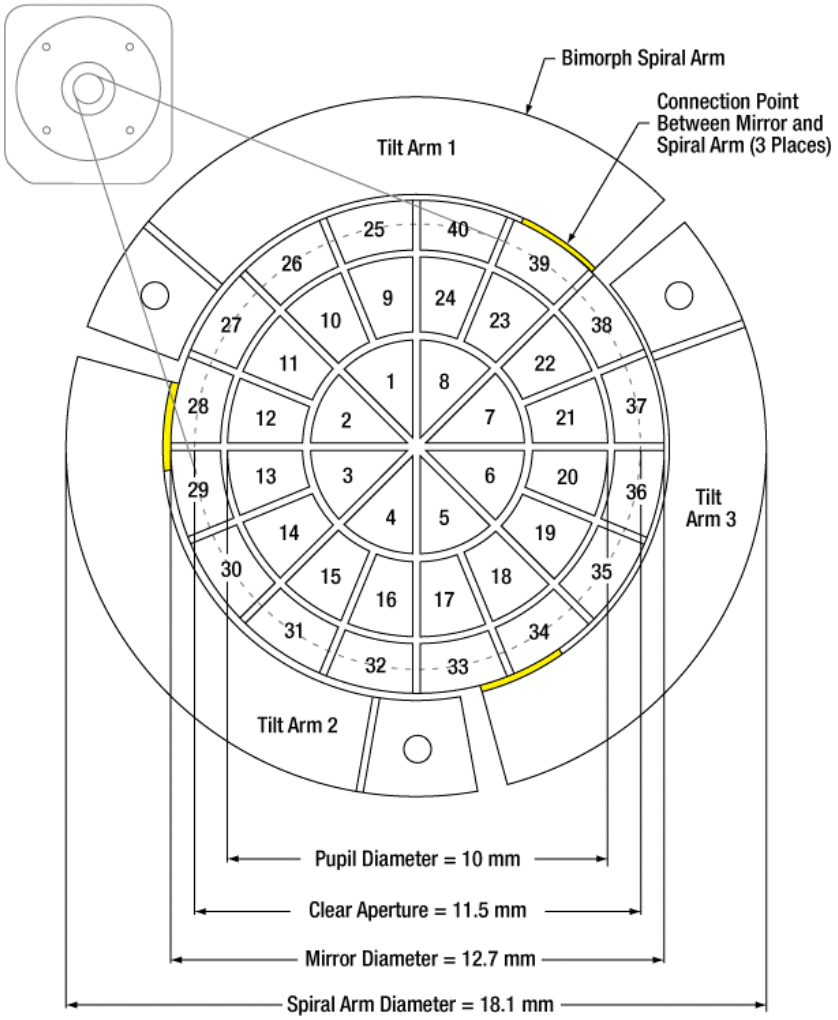

Figure 4.12: Diagram of the Thorlabs deformable mirror used to counteract imperfections in the parabolic mirror's surface. *Image credit: Thorabs[4]*

of 2.1 μm but still 2.8 times larger than the diffraction limited spot size of 0.61 μm.

4.3.3 Micromotion

With defocusing and imaging issues ruled out, we determined mircromotion to be the next most likely candidate for our large spot size. As discussed in section 3.3, trapped ions undergo oscillation while trapped. The ion's motion in one dimension can be approximated as:

$$x(t) = [x_0 + x_1 cos(\omega t)][1 + \frac{q}{2} cos(\Omega t)] \tag{4.2}$$

where x_0 is the ion's displacement from the center of the trap due to constant voltage offsets, x_1 is the maximum amplitude of the ion's oscillation in the RF psuedopotential well, ω is the secular frequency of the trap ($\omega = 2\pi \times 0.3$ MHz for our system in the radial direction), q is a dimensionless constant related to the RF field and trap geometry ($q \approx 0.1$ in this case, discussed more in Sec. 3.3.1), and Ω is the RF driving frequency ($\Omega = 2\pi \times 12$ MHz for this experiment).

The ion undergoes micromotion at a frequency Ω. The amplitude of this motion increases as the ion moves further away from the RF null (i.e. as x_0 increases). By using the bias plates to place the ion at the optical focus of the trap, we are moving it out of the RF minimum. The ion was displaced radially $\sim$40 μm, giving a micromotion amplitude of $x_0 \times q/2 \approx 2$ μm.

Secular motion is the other component of the ion's behavior. It is slower than the micromotion by a factor of about 40. Doppler cooling (Sec. 3.3.2) can reduce the amplitude of this motion to $x_1 = \sqrt{\hbar\Gamma/m\omega^2} \approx 0.3\mu m$, where Γ is the natural linewidth of the excited state used ($6P_{1/2}$, $\Gamma \approx 2\pi \times 10$ MHz) and m is the mass of the ion used ($m = 137.9$ u for barium).

The secular motion amplitude is still smaller than the diffraction limit (0.61 μm), so it doesn't explain the ion's large spot size. The amplitude of the micromotion, on the other hand, at 2 μm is consistent with the spot size of 1.7 μm seen when the deformable mirror was used.

Micromotion occurs in multiple dimensions, explaining why our final spot size differs from the calculated 2 μm. Additionally, the four bias plates used to displace the ion induce a field which is not radially symmetric, causing the final ion image to not simply take the form of an ellipse along the direction of displacement.

Further support for this conclusion was acquired by measuring the ion spot size at different NAs by using the calibrated iris on the ion's light after it reflected from the parabolic mirror. There were no noticeable changes to the ion image spot size as the NA was reduced, indicating that diffraction and imperfections in the mirror were not to blame for its large size.

4.3.4 Radial control of needle

To minimize the micromotion experienced by the ion at the focus of the mirror, we needed to have the focus coincide with the minimum of the RF pseudopotential.The first iterations of the parabolic mirror trap moved the ion radially through the use of bias plates mounted above the opening of the mirror (Figs. 4.4, 4.5). However, this induces micromotion, as discussed in the section above. A new radial positioning system was designed by a former graduate student, Carolyn Auchter, which flexes the needle to radially position the ion instead of introducing a DC bias field (Fig. 4.13). In her design, the needle was held firmly at one end and a force was applied about 2/3 of the way to the needle tip which flexed the needle. This force was applied by a piezo and a spring acting in opposition, and there were two piezo+springs sets at different axial locations to provide flexing in two orthogonal directions.

This design was revamped by myself and fellow graduate student Alex Kato. The grounded needle in the existing component had become misaligned relative to the axis of the parabolic mirror, such that it would not be possible to center an ion in the trap. Upon breaking vacuum and investigating, it was discovered that there were reproduceability issues with the design in its original form. The surface of the piezo and the top of the spring rested directly on the needle. This allowed slight shifting to occur in where the point of contact was, leading to the needle misalignment. Additionally, the spring and piezo both have flat bottoms but were stored in rounded slots. This allowed the spring to shift slightly over time as it did not sit well in its slot. Furthermore, the forces for the two orthogonal directions of motion were applied at different axial locations, causing one direction to have greater movement than the other for the same applied piezo force.

To address these issues, we took two main actions with the new design (Fig. 4.14, 4.15). First, both sets of piezos and screws acted on the needle at the same axial location, allowing for more

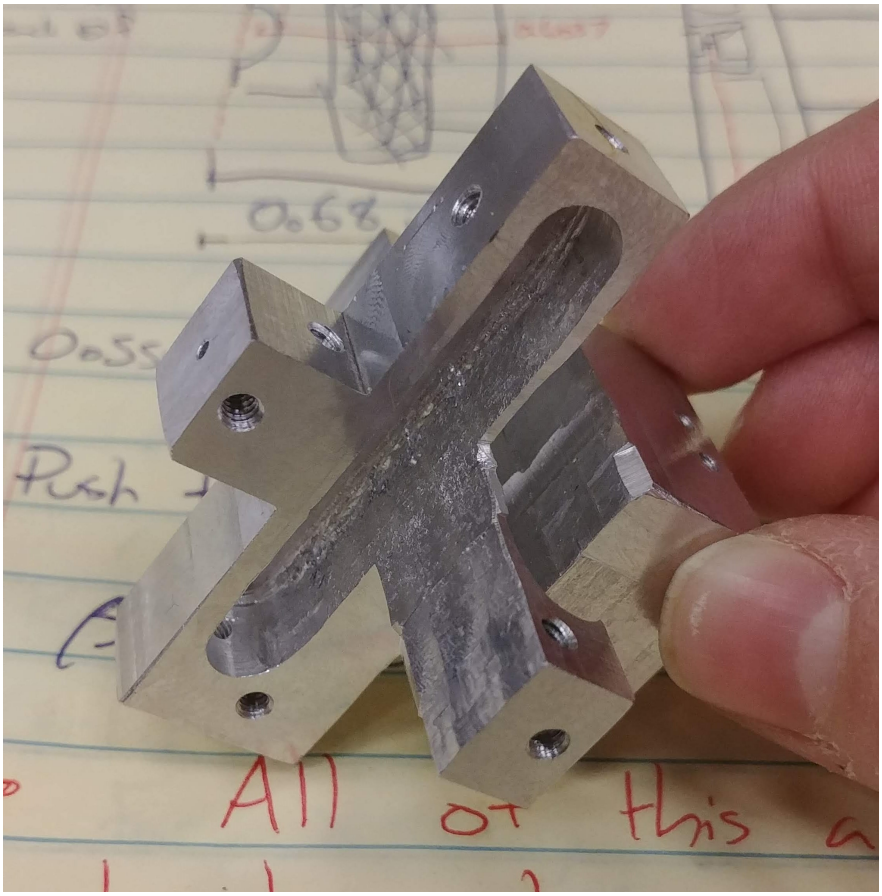

Figure 4.13: Original part used to flex needle. The base of the needle emerged through the small hole on the left of the part. The base plate (held by hand) attached to the base trap where there was a hole for the tip of the needle to go through the base of the parabolic mirror. Two slots were used to hold a piezo and a spring each, which worked in opposition to flex the needle.

uniform motion. Second, set screws were used to secure the needle within a small block that the springs and piezos pushed on. This allowed their force to be exerted at a small, fixed location on the needle, increasing reproduceability.

The grounded needle was flexed with a combination of piezos and springs. The needle was mounted on a holder attached to two guide rods emerging from the base plate of the trapping assembly. The holder had a cross carved into it centered around the needle. A piezo and a spring were installed in opposition in the two orientations of the cross (Fig. 4.14). Applying voltage to

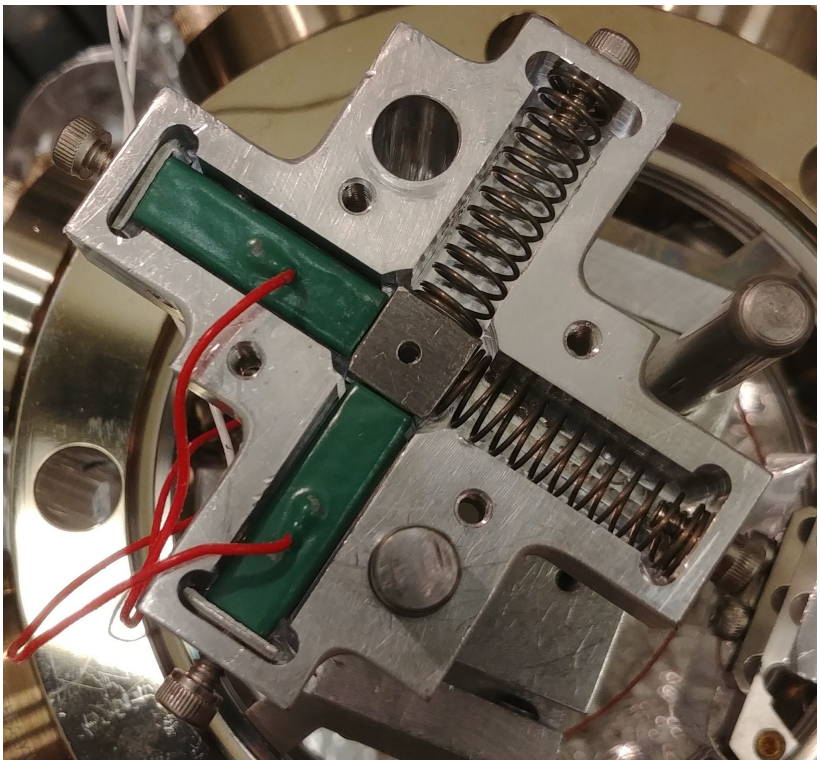

Figure 4.14: New needle flexing trap component. Piezos (green) mounted in needle flexing piece. When installed, the needle emerges from the center hole. It is secured inside the center block by a pair of set screws, and within the holder by another set, allowing for movement of the small block to flex the needle. The two springs oppose the piezos, allowing for movement in all radial directions. The piece slides along a pair of guiderods (more clear in Fig. 4.15) through a pair of slip fit holes. In this image, one hole is mounted while the other is not. The set screws at the end of the piezo containing slots allow for coarse centering of the needle at half voltage, and the set screws in the center of the springs prevent them from vacating the apparatus at high velocity while the lid (not shown) is not present.

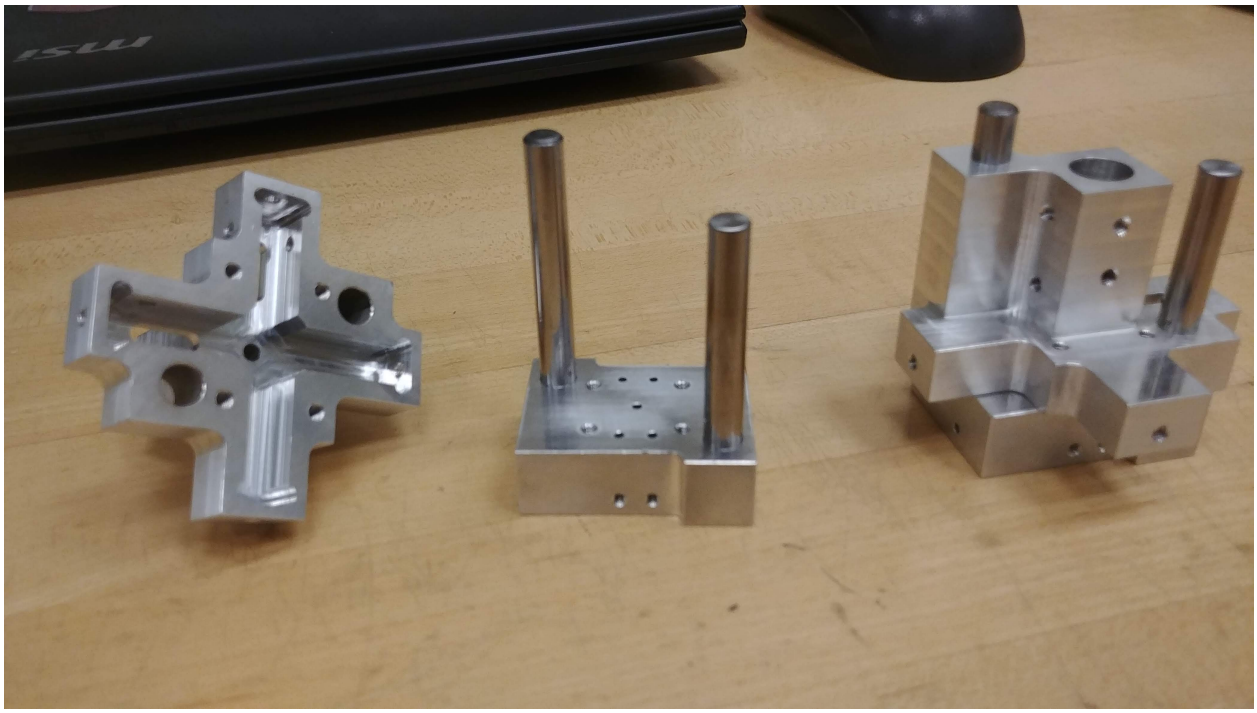

Figure 4.15: Left) The piezo holder. Middle) Base plate which attached to trap apparatus base. Two guide rods were used to align the piezo holder. Right) Assembled apparatus.

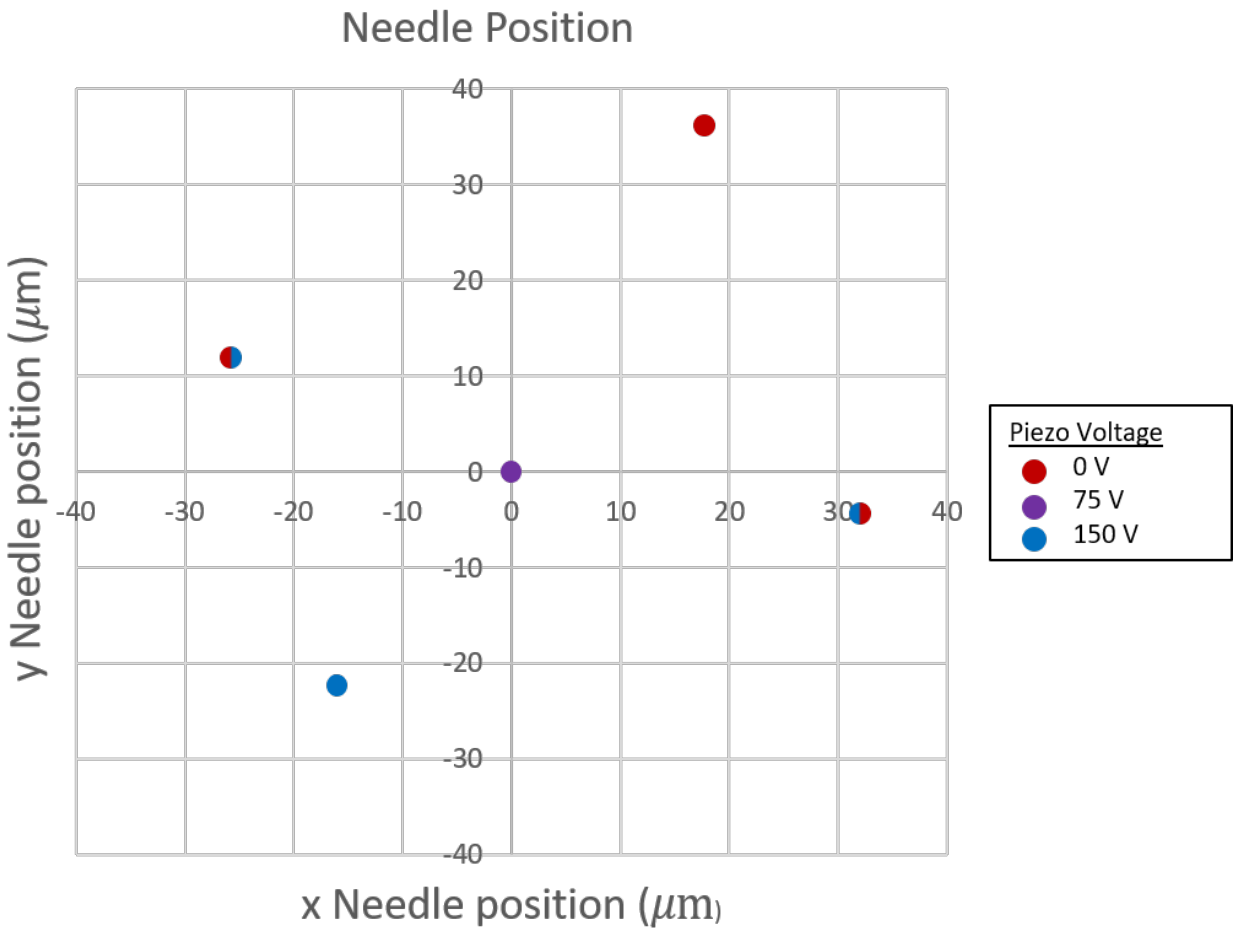

Figure 4.16: Measured needle movement due to piezo forces. The needle moved 27-40 μm, depending on the voltage applied to the piezos.

the piezo stack increased its length, which pushed on the needle and flexed it away. The system was aligned with the piezos at half-max extension (75 V), such that by decreasing the voltage the spring would force the needle to flex in the direction of the piezo stack, allowing full radial control of 27-40 μm in the needle location. The actual displacement of an ion at the focus of the trap is expected to follow.

In the earlier investigations, the ion needed to be displaced about 40 μm to reach the optical focus of the trap. As part of installing the new component, the trap was rebuilt and the relative

alignment of the needle and mirror, as well as the location of various stray fields, will have shifted. However, the amount of correction needed is likely to be of approximately the same amount. In which case, we could need 40 μm of movement in the weakest direction of needle control (27.2 μm). This will result in using the bias plates to move the ion the remaining 12.8 μm. This gives a micromotion amplitude of $x_0 \times q/2 \approx 2 = 0.64$ μm, which is only 1.05 times larger than the diffraction limited spot size of 0.61 μm.

4.3.5 Polarization

The parabolic mirror alters the polarization of reflected light, allowing it to be used for polarization filtering when reflected light is fiber-coupled into a single-mode optical fiber. Applying an external magnetic field to a trapped ion introduces Zeeman sublevels, allowing transitions with $\Delta l = 1$ and $\Delta m = \pm 1$ to occur. The photons emitted from these transitions are polarized, with optical fields given by

$$\vec{E}_{\Delta l=1,\ \Delta m=0} = E_0 \frac{ie^{ikr}}{r} \sqrt{\frac{3}{8\pi}} sin(\theta)\hat{\theta} \tag{4.3}$$

$$\vec{E}_{\Delta l=1,\ \Delta m=\pm 1} = E_0 \frac{ie^{ikr}}{r} e^{\pm i\phi} \sqrt{\frac{3}{16\pi}} (\pm cos(\theta)\hat{\theta} + i\hat{\phi}) \tag{4.4}$$

where E_0 is the amplitude of the electric field, k is the wave number [20, 21] and the axes are defined in Figure 4.17. Field intensity plotted in Figure 4.18.

To calculate the effect of the mirror on polarization and fiber coupling, we need to calculate the post-reflection optical field. Post-reflection intensity will depend solely on ρ (distance from the z axis; see Fig 4.17 for coordinate system), so the angular components of Eq. 4.3-4.4 must be converted. Figure 4.19 shows the effect of the mirror on three sample rays, and from the image it's clear we need a mapping between the angle of emission (θ) and the post-reflection radial distance, ρ. The equation for the paraboloid forming the surface of the mirror is given by Eq. 4.1 with a focus of 2 mm.

For a general focal length, the relation between angle of emission and reflected photon's dis-

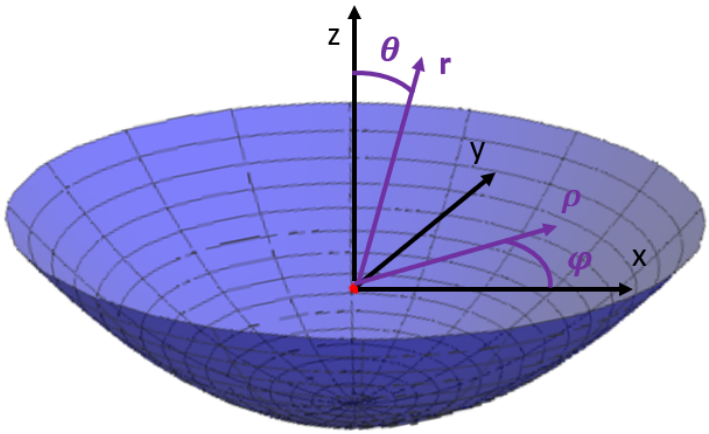

Figure 4.17: Coordinate system used when calculating polarization upon reflection from the parabolic mirror (blue surface defined by Eq. 4.1). The ion (red) is located at the center of the coordinate system and the focus of the parabolic mirror. The magnetic field, and thus quantization axis, is along the optical axis, $\hat{z}$.

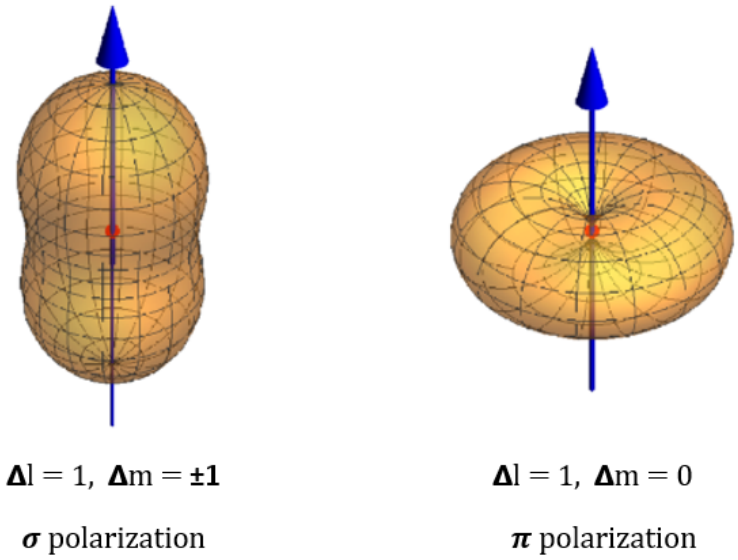

Figure 4.18: Angular probability distributions for photons emitted from an ion (red point) with the magnetic field direction indicated by the blue arrow. Distance from the ion corresponds to emission probability.

tance from the z axis (ρ) is calculated to be

$$\theta = sin^{-1}\left(\frac{4f\rho}{\rho^2+4f^2}\right), \tag{4.5}$$

and the distance from the origin to the surface of the parabolic mirror (r) is:

$$r = \left(\frac{1}{4f}\right)(\rho^2+4f^2). \tag{4.6}$$

Upon reflection, polarization in the azimuthal direction $\hat{\phi}$ is unaffected, but $\hat{\theta}$ becomes oriented in $-\hat{\rho}$. Making these changes in Eq. 4.3-4.4 leads to

$$\vec{E}_{\Delta l=1,\ \Delta m=0} = -iE_0\rho e^{ik\left(\frac{\rho^2+4f^2}{4f}\right)}\left(\frac{2f}{\rho^2+4f^2}\right)^2\sqrt{\frac{6}{\pi}}\,\hat{\rho} \tag{4.7}$$

$$\vec{E}_{\Delta l=1,\ \Delta m=\pm 1} = E_0\left(\frac{\pm if}{\rho^2+4f^2}\right)e^{ik\left(\frac{\rho^2+4f^2}{4f}\right)}e^{\pm i\phi}\sqrt{\frac{3}{\pi}}\left(\frac{\rho^2-4f^2}{4f^2+\rho^2}\hat{\rho}\pm i\hat{\phi}\right). \tag{4.8}$$

These intensity profiles are plotted in Fig. 4.20.

Calculating the mode overlap will show how much of this light couples into a single mode optical fiber. The mode overlap is given by [21]

$$T_{l,m} = \frac{|\int_0^{2\pi}\int_0^{\rho_0} d\phi d\rho\rho\vec{E}_{l,m}\cdot\vec{G}|^2}{\int_0^{2\pi}\int_0^{\infty} d\phi d\rho\rho\vec{E}_{l,m}\cdot\vec{E}_{l,m}\int_0^{2\pi}\int_0^{\infty} d\phi d\rho\rho\vec{G}\cdot\vec{G}} \tag{4.9}$$

where ρ_0 is the opening radius of the mirror (5.1 mm in our case) and the Gaussian mode of the optical fiber is

$$\vec{G} = e^{-\left(\frac{\rho}{w}\right)^2}(\alpha\hat{x}+\beta\hat{y}) = e^{-\left(\frac{\rho}{w}\right)^2}[(\alpha cos(\phi)+\beta sin(\phi))\hat{\rho}+(\beta cos(\phi)-\alpha sin(\phi))\hat{\phi}] \tag{4.10}$$

for $|\alpha|^2+|\beta|^2=1$ where w is the Gaussian beam waist (radius where beam intensity is $1/e^2$ the maximum intensity).

Calculating the mode overlap for π polarized light (Δm=0) reveals that none of the light is fibercoupled. From Eq. 4.7, we see that the field has no ϕ dependence. The integral over ϕ in the numerator goes to zero, and therefore we see there is no mode overlap.

For σ polarized light, on the other hand, we find

$$T_{1,\pm 1} = \frac{3}{2}\left(\frac{2f}{w}\right)^6|\alpha\pm i\beta|^2 e^{2(2f/w)^2}\left|\Gamma\left(-1,\frac{4f^2}{w^2}\right)-\Gamma\left(-1,\frac{\rho_0^2+4f^2}{w^2}\right)\right|^2. \tag{4.11}$$

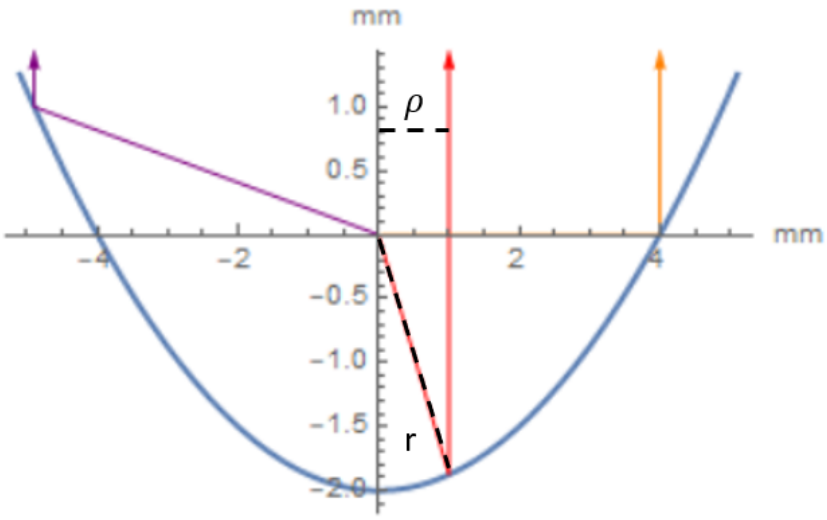

Figure 4.19: Light emitted from a source at the focus of a paraboloid is reflected in a collimated beam. Image displays a schematic of three light rays emitted from an ion at the focus of the parabolic mirror. Scale is in mm, and r and ρ have been labelled with dashed lines on the red sample light ray.

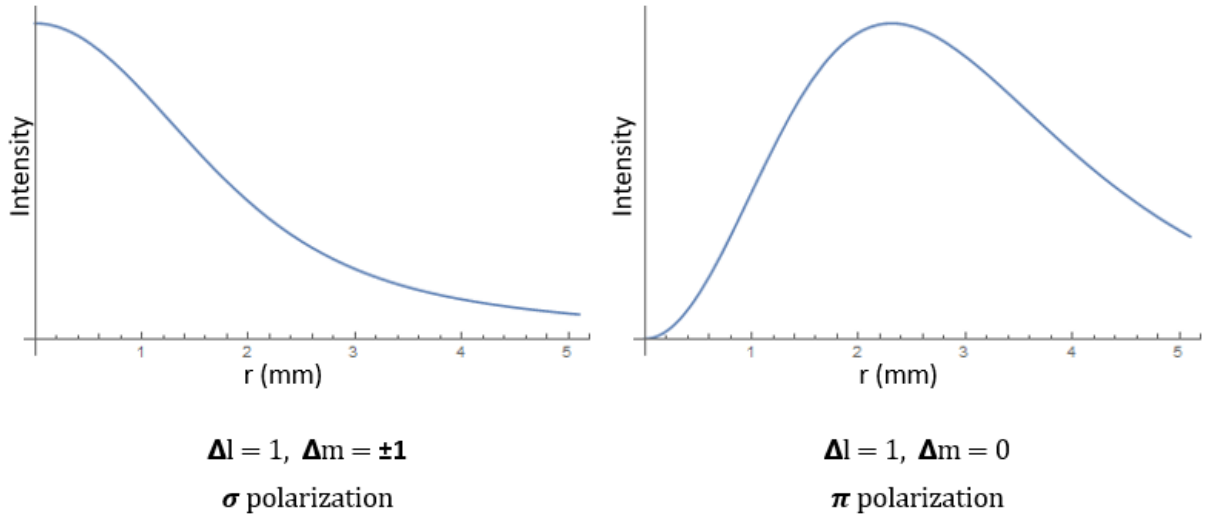

Figure 4.20: Intensity profile of fields reflected from the parabolic mirror depends only on the distance from the axis. Horizontal scale is mm from axis, and extends to 5.1 mm; the radial size of the mirror opening.

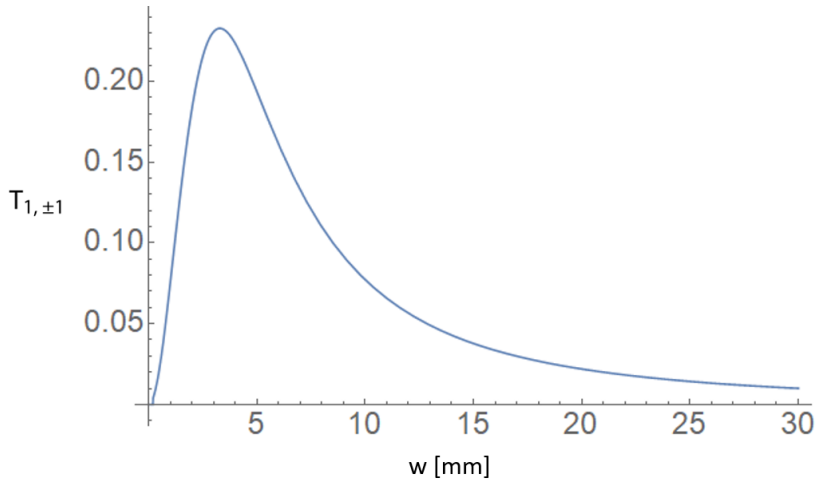

Figure 4.21: Probability of fibercoupling light from a σ^+ or a σ^- transition as a function of Gaussian mode waist, w.

Our parabolic mirror trap was constructed with a focal length of 2 mm and an opening radius of 5.1 mm. Using these values, we find that the maximum fiber-coupling efficiency of 23% of σ^+ or σ^- polarized light is attained when our Gaussian mode waist w=3.3 mm (Fig.4.21).

A fiber with a 3.3 mm radius Gaussian mode is not standard optics equipment by any stretch of imagination. Standard optical fibers have a waist of $\sim$3 μm. This large waist will need to be focused down with a lens in order to couple it into the fiber. The required lens can be calculated with

$$\alpha = \frac{f}{\sqrt{(|s|-f)^2 + z_R^2}} \tag{4.12}$$

where f is the lens focal length, s is the distance between the lens and the unfocused Gaussian mode waist, α is the magnification of the beam waist, and z_R is the Rayleigh range, $z_R = \pi w_0^2/\lambda$.

The two ions discussed in this body of work are Yb^+ and Ba^+, and the photons collected from those systems have wavelengths of 369 nm and 493 nm, respectively. To focus a 3.3 mm Gaussian waist down to 3 μm requires a lens of focal length 25.5 mm for Yb^+ and 19.1 mm for Ba^+. These results are largely independent of the distance between the original waist w_0 and the lens because the original beam is so large that it diverges slowly.

Chapter 5

BARIUM OVEN CONSTRUCTION

An ion trap is nothing without ions to be trapped. For our system, this was accomplished by the incorporation of a resistively heated tube containing a sample of metallic barium. The atomic beams were ionized by a combination of 337 nm and 791 nm light. Generating ions in this manner can produce all isotopes of the relevant element proportional to their natural dependence. Isotope selection is then performed through tuning the ionization laser (Fig. 5.1).

When making adjustments to the parabolic mirror trap, vacuum had to be broken. Atomic barium oxidizes readily in air, so this process rendered the installed barium oven useless. Additionally, the oven tube itself must be replaced, as lingering barium oxide can cause issues with newly loaded barium leading to oven failure.

5.1 Oven Construction

We tried an assortment of tube sizes and thicknesses, and found that stainless steel tubes of wall thickness 0.13 mm, 3 mm diameter, and length $\sim$1.5 cm performed best for barium ovens. Thinner tube walls would melt at the high currents needed to break through the oxidation layer on the surface of atomic Ba. Shorter ovens required more current to heat effectively and connections would fail before the oven activated. Ovens which were too long had the pressure within the tube sufficiently high such that the mean free path of the evaporated Ba was too short for it to escape the confines of the oven.

Constructed ovens needed to be preactivated at high current (60+ W) for approximately an hour at low vacuum to remove water and other contaminants which could react with the loaded Ba. Clean ovens were transferred from the trap to low oxygen environments as rapidly as possible to prevent them from becoming dirty again.

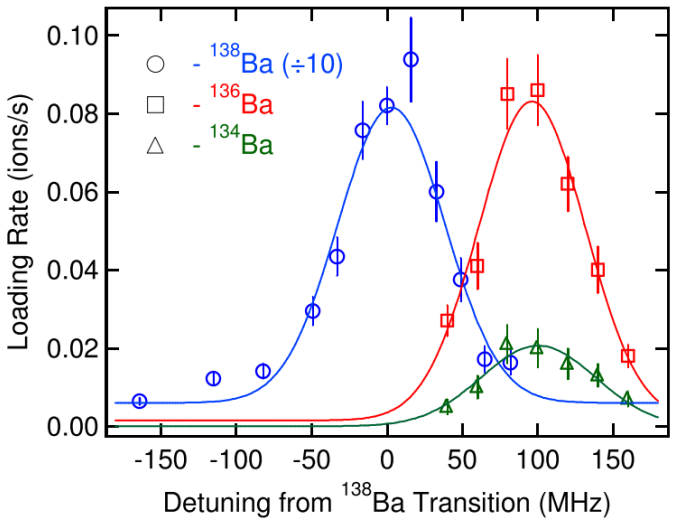

Figure 5.1: Barium ionization rate at different ionization laser frequencies. Barium 138 is far more prevalent than the other isotopes, and tuning the 791 nm ionization laser allows for it to be ionized almost exclusively. Figure from Steele *et al.*[5]

5.2 Oven Loading

An additional difficulty when constructing Ba ovens is the reactivity of the subject material. Barium reacts readily with oxygen, so loading must be done in a low oxygen environment. Two strategies were used to accomplish this. The first was to use aluminum foil to construct a tub within the bakeout oven, and then use dry ice to displace the air within the tub with CO_2. The open trap was placed within the tub and connected to the vacuum pumps, and barium could be cut and loaded into the tube and trap all within the bath. Drawbacks of this method include difficulty loading, as this must be accomplished from above the top of the high tub walls without disturbing the gas within, and a slight reactivity between Ba and CO_2, leading to failed ovens when loading took too long.

Eventually, as glove bag was constructed out of plastic sheeting and nitrile gloves (Fig. 5.2). Inert gases, such as argon or nitrogen, were piped into the sealed bag and loading performed within that inert environment. Loaded ovens were sealed with indium foil and rapidly loaded onto the trap

Figure 5.2: A glovebag was constructed to allow barium loading in an inert neutral gas. Gloved hands inserted into the attached XL gloves allowed for dexterous manipulation of the barium sample and oven. Tubing attached to the right corners of the bag allowed it to be filled from a gas cannister and pumped out with a roughing pump. A strip of tape on the backside of the bag (not visible) was used to seal a slit used for inserting and removing components.

and pumped down. Difficulties with this method include properly sealing the oven tubes with In and issues with the In plug removal. Indium melts at a much lower temperature than Ba, so a relatively low current (<8 W) could be run through the oven once at low pressure to encourage the indium's removal, but the indium splatters could cover inconvenient surfaces. Incomplete sealing would allow oxygen into the tube when transferring it to the trap and render the Ba useless. We tested the efficacy of different cleaning treatments of the In before sealing to increase its stickiness by removing the oxide layer, and found that on the timescales we needed the system to be sealed, removal of the indium oxide was not required for efficient sealing.

5.3 Oven Activation

Not matter how rapidly the ovens were loaded or transferred to the trap, some oxide would form on the surface of the Ba which needed to be removed. Systems would be pumped down, then increasing currents run through the tube until a Ba spray was noticed. Surfaces within the trap, such as the shield, would be monitored for a Ba shadow. The operation current was then several amps below the current at which the Ba shadow appeared. Values at which this shadow appeared varied with oven construction but activation power tended to be approximately 35 W (18 A), and corresponding operation power <8 W (8 A), depending on the desired loading rate.

5.4 Oven Alignment

The direction of the atomic beam emitted from the oven must pass through the trapping region of the assembled trap. Alignment was accomplished through different methods for the different systems. In the original parabolic mirror trap, alignment could be accomplished by installing a shield over the opening of the oven tube with a small aperture. Atomic Ba would be collimated by the combination of the oven tube opening and the shield aperture.

Improper shielding of the barium oven source lead to a barium buildup on one of the support pins for the trap. Eventually, the barium layer was sufficient to ground the parabolic mirror surface, removing the RF potential required for trapping. This problem revealed itself in increased trap pressure from the layer heating as RF current ran through it and an increase in background photon counts from the heated barium layer emitting blackbody radiation. Further investigation with a multimeter revealed that the RF connection was grounded.

A high wattage (up to 4 W after amplifier and accounting for RF coupling) applied through the RF input was able to evaporate the barium layer. Such a layer should not form during traditional trap operation, as the oven is on for shorter periods of time and the barium deposits are removed by standard RF operation powers.

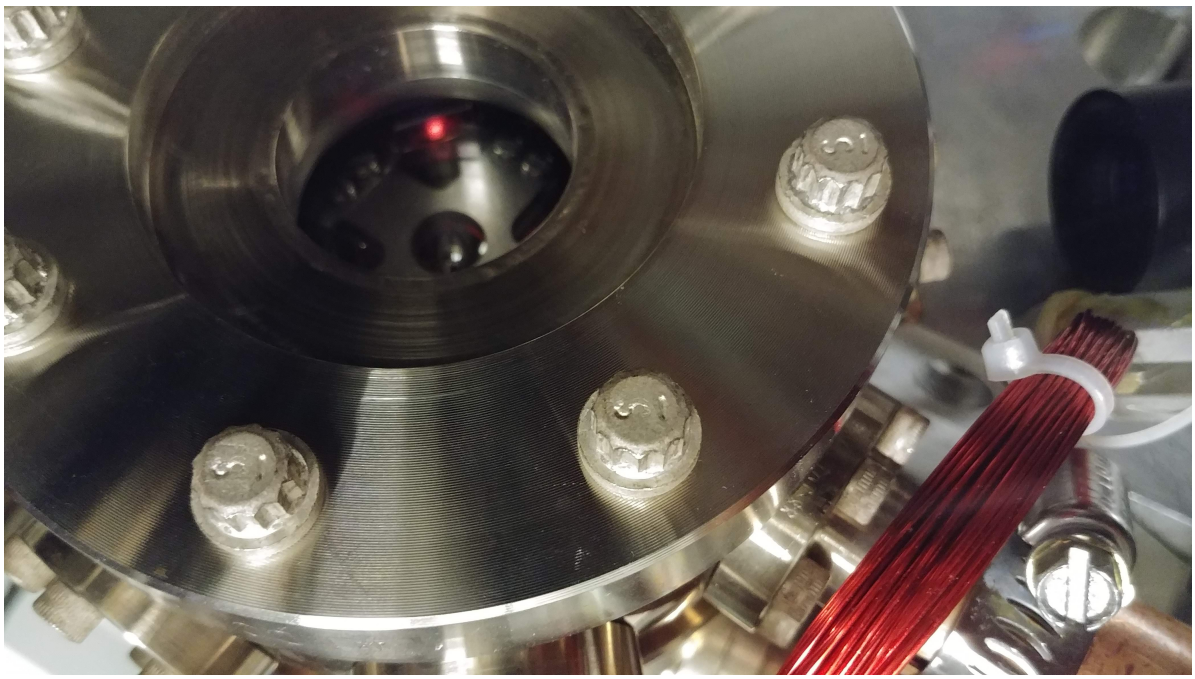

Figure 5.3: High RF current was used to evaporate the barium layer connecting the mirror to ground. The barium layer can be seen glowing through the front viewport of the trap.

Chapter 6

REMOTE ENTANGLEMENT SCHEME BETWEEN A SOLID-STATE SEMICONDUCTOR DEFECT AND A TRAPPED ION

6.1 Introduction

Hybrid quantum systems offer the opportunity to combine the benefits of different qubit types while avoiding some of their pitfalls. Task-dependent qubit selection allows the usage of long-lived qubits for memory and qubits with rapid gate speeds for operations. For optical systems, a photon bus can be used to remotely link these systems via photon-heralded entanglement. To successfully generate entanglement, the two different qubit systems must emit identical photons, requiring spectro-temporal engineering of at least one qubit's photon wavepacket. While significant progress has been made toward efficient quantum-frequency conversion [22, 23, 24, 25], post-emission temporal photon pulse-shaping [26, 27, 28] techniques for the narrow-band photons from both trapped ions and solid-state defects is an outstanding challenge.

We have identified two disparate, complementary qubit systems in which high-fidelity photon-mediated entanglement should be possible by direct control over the photon emission process. Trapped ions are a well-studied qubit system with high operational fidelities and long coherence times [29], but relatively slow initialization and gate speeds [30]. Electron spins in semiconductors have rapid initialization and gate speeds [31, 32, 33], but have shorter coherence times. A hybrid system consisting of ions and electrons bound to donor defects would have the ability to use ions for quantum memory and defects for gate operations, producing a system more rapid and reliable than either qubit alone.

Yb^+ and the ZnO donor were chosen as the target systems for their shared transition near 369 nm: the $^2P_{1/2}$ to $^2S_{1/2}$ transition in $^{171}Yb^+$ and the In neutral donor bound exciton (D^0X) to neutral donor (D^0) transition in ZnO (Fig. 6.1). In:ZnO is analogous in structure to the better-

known P:Si qubit system [34], however ZnO is a direct band gap semiconductor enabling efficient donor coupling to photons. While the two transition frequencies are quite close (δ = 340 GHz), the excited state lifetimes differ by a factor of 6 resulting in a large temporal mismatch. Prior semiconductor spin - trapped ion entanglement schemes addressed similar temporal mismatch by using coherent scattering [35] or sacrificing fidelity [36]. Here we demonstrate that pulse shaping can be a powerful tool to attain high-fidelity entanglement and show that an entanglement rate of 21 kHz and fidelity of 94% is feasible.

6.2 Experimental Scheme

A heralded entanglement scheme based on weak excitation, single-photon detection and which-path erasure can be used to entangle the two systems, similar to the proposal by Cabrillo *et al.* [10] Fig. 6.1 depicts the relevant energy levels and excitation/decay pathways for the donor and ion. Here D^0 system is in the Voigt ($B\perp \hat{k}$) geometry but the Faraday ($B\| \hat{k}$) geometry could also be utilized. The geometry used effects the decay channel chosen by the exciton from the excited level, with Voigt geometry leading to 50/50 splitting between H and V polarization. The donor is coupled to an optical cavity detuned by Δ from the D^0X-D^0 transition.

The diagram of the experiment is shown in Fig. 6.2. The Yb^+ and In donor are first initialized using optical pumping to $|F=0,m_F=0\rangle$ and $|m_s=-1/2\rangle$, respectively, producing the initial state $|\Psi\rangle_i = |0\rangle_{\mathrm{Yb}} \otimes |0\rangle_{\mathrm{In}} \otimes |\mathrm{vac}\rangle \equiv |0;0;\mathrm{vac}\rangle$. Next, each system is excited to $|e\rangle_{\mathrm{In}}$ or $|e\rangle_{\mathrm{Yb}}$, using resonant or near-resonant pulsed excitation. Here, we assume the weak excitation limit (excitation probability $p_{1,x} < 10\%$, $x = \{\mathrm{Yb,In}\}$). The state of the ZnO donor and ion is now given by

$$\begin{aligned} |\Psi\rangle_c = \beta_1 |0;0;\mathrm{vac}\rangle + \beta_4 |1;1;\zeta_{\mathrm{Yb}},\zeta_{\mathrm{In}}\rangle + \\ + \beta_2 |0;1;\zeta_{\mathrm{In}}\rangle + \beta_3 |1;0;\zeta_{\mathrm{Yb}}\rangle , \end{aligned} \tag{6.1}$$

where the emitted photons on paths A and B of Fig. 6.2 are $|\zeta_{\mathrm{Yb}}\rangle = \sum_\omega \xi_{\mathrm{Yb},\omega}\, \mathrm{a}^\dagger_\omega |\mathrm{vac}\rangle$ and $|\zeta_{\mathrm{In}}\rangle = \sum_{\omega'} \xi_{\mathrm{In},\omega'}\, \mathrm{b}^\dagger_{\omega'} |\mathrm{vac}\rangle$, given by a sum over all modes ω (ω') with coefficients $\xi_{\mathrm{Yb},\omega}$ ($\xi_{\mathrm{In},\omega'}$) and creation operators $\mathrm{a}^\dagger_\omega$ ($\mathrm{b}^\dagger_{\omega'}$). The coefficients β emerge from the excitation ($p_{1,x}$) probabilities of the two systems, the phase gained from excitation laser phases ($\phi_{x,L}$), and the distance travelled by

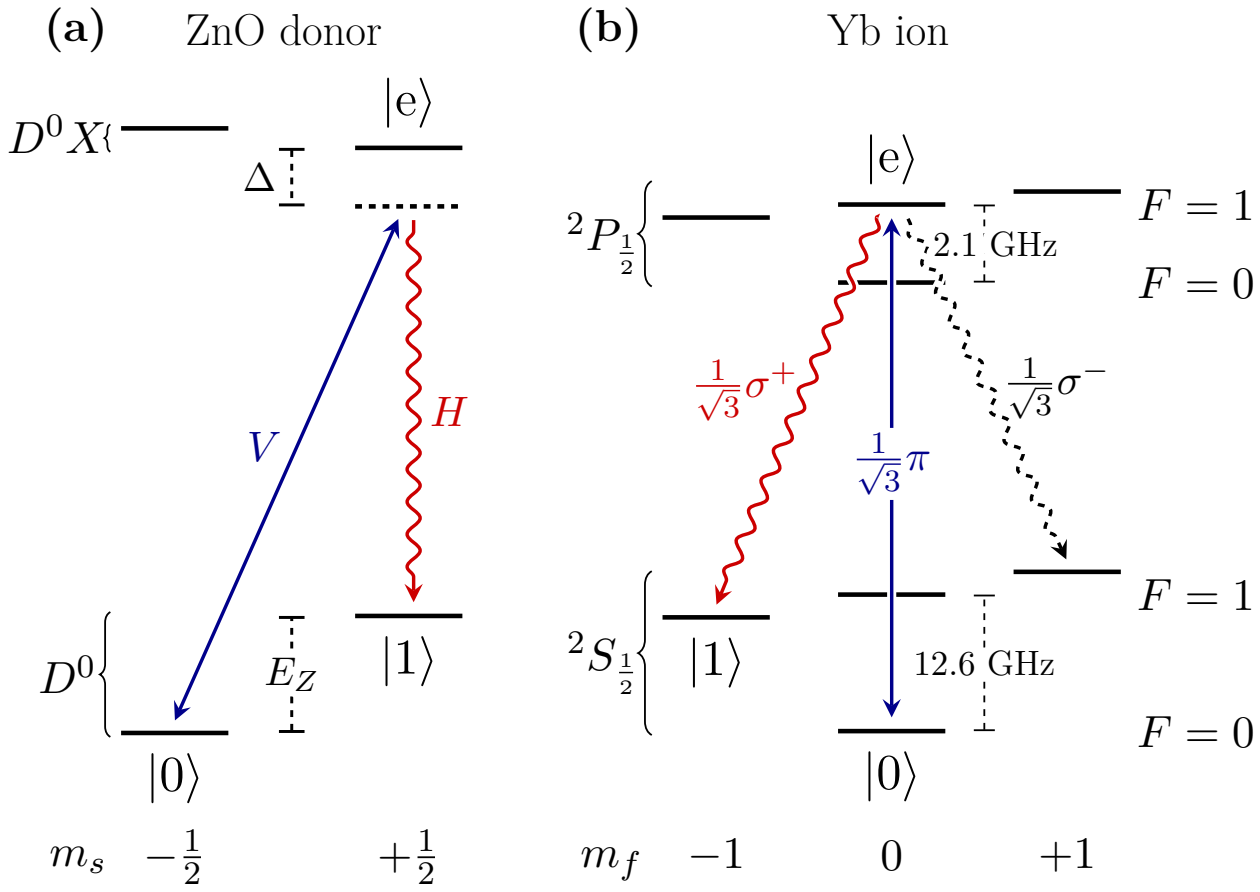

Figure 6.1: Partial energy level diagrams of ZnO donor (a) and $^{171}Yb^+$ (b). The qubit system in ZnO is comprised of the two electron spins ($|0\rangle$ and $|1\rangle$) of the neutral donor D^0. This state is optically coupled to the donor-bound-exciton state D^0X consisting of the donor, two-electron spin singlet, and hole. The $^{171}Yb^+$ qubit is formed by the $|F=0,m_F=0\rangle$ and $|F=1,m_F=-1\rangle$ hyperfine levels in the $^2S_{1/2}$ ground state. The magnetic field in ZnO system is set such that the Zeeman splitting E_Z is an integer multiple of the qubit transition in Yb^+.

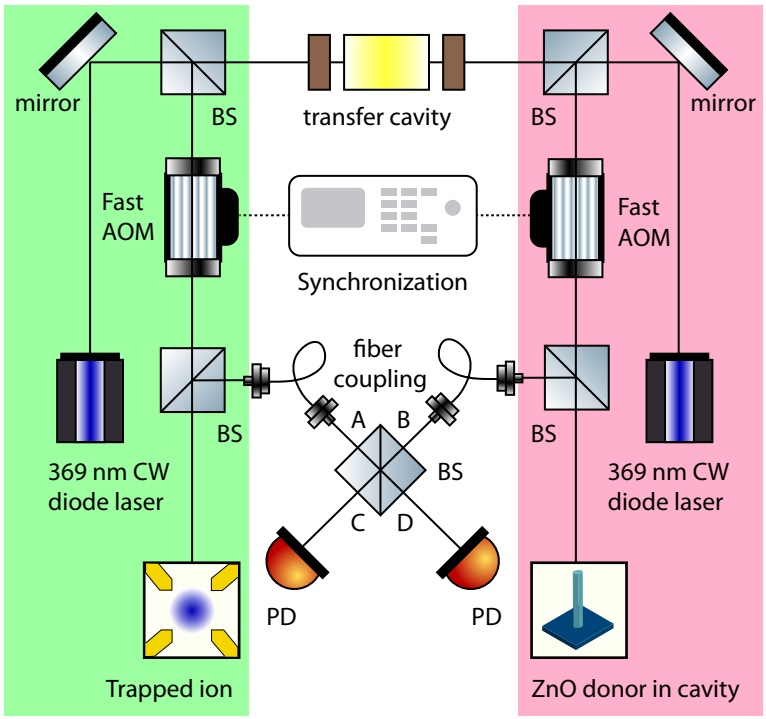

Figure 6.2: Trapped ion system (left) and ZnO system (right). A transfer cavity phase-locks the two 369 nm excitation lasers. The two acousto-optic modulators (AOM) are synchronized and programmed to output the calculated pulse shapes for their respective qubits. Photons collected from the two qubits interfere on the beam splitter (BS) via inputs A and B. Successful entanglement is heralded by the detection of a single photon by photodetectors (PD) at outputs C, D. *Image credit: Xiayu Linpeng*

the collected photon ($\phi_{x,d}$):

$$\begin{aligned}
\beta_1 &= \sqrt{(1-p_{1,\mathrm{Yb}})(1-p_{1,\mathrm{In}})}e^{i(\phi_{\mathrm{Yb},L}+\phi_{\mathrm{In},L})} \\
\beta_2 &= \sqrt{p_{1,\mathrm{In}}(1-p_{1,\mathrm{Yb}})}e^{i(\phi_{\mathrm{Yb},L}+\phi_{\mathrm{In},d})} \\
\beta_3 &= \sqrt{p_{1,\mathrm{Yb}}(1-p_{1,\mathrm{In}})}e^{i(\phi_{\mathrm{Yb},d}+\phi_{\mathrm{In},L})} \\
\beta_4 &= \sqrt{p_{1,\mathrm{In}}p_{1,\mathrm{Yb}}}e^{i(\phi_{\mathrm{Yb},d}+\phi_{\mathrm{In},d})}
\end{aligned} \tag{6.2}$$

By phase locking the laser pulses, we can ignore $\phi_{x,L}$.

Our goal is to have two equally indistinguishable possibilities for the ion and donor states. For this to occur, we need to have an equal probability of detecting a photon from either system. By balancing the collection and emission probabilities,

$$p_{1,\mathrm{Yb}}(1-p_{1,\mathrm{In}})p_{2,\mathrm{Yb}} = p_{1,\mathrm{In}}(1-p_{1,\mathrm{Yb}})p_{2,\mathrm{In}}, \tag{6.3}$$

we can accomplish this goal. This will put our wavefunction into a maximally entangled Bell state which normalizes to

$$|\Psi\rangle = \frac{1}{\sqrt{2}}(|0;1+|1;0\rangle\rangle) \tag{6.4}$$

Since we use the excitation probability, $p_{1,x}$, to achieve good temporal overlap, and typically the collection efficiency for donors is greater than that of trapped ions ($p_{2,\mathrm{Yb}} < p_{2,\mathrm{In}}$), the relation given in Eq. 6.3 is accomplished by lowering the collection efficiency of the ZnO system, $p_{2,\mathrm{In}}$.

Now, at the beamsplitter we choose the transformations:

$$\mathrm{a}^\dagger_\omega \rightarrow (\mathrm{c}^\dagger_\omega + i\,\mathrm{d}^\dagger_\omega)/\sqrt{2} \tag{6.5}$$

$$\mathrm{b}^\dagger_{\omega'} \rightarrow (\mathrm{d}^\dagger_{\omega'} + i\,\mathrm{c}^\dagger_{\omega'})/\sqrt{2} \tag{6.6}$$

where $\mathrm{a}^\dagger_\omega$, $\mathrm{b}^\dagger_{\omega'}$ are the raising operators of the respective paths A and B and $\mathrm{c}^\dagger_\omega$, $\mathrm{d}^\dagger_\omega$ are the raising operators in paths C and D, as depicted in Fig. 6.2.

We also have that $i(\phi_{D_2} - \phi_{D_1}) = i\Delta\phi$ where $\Delta\phi$ is the difference in phase between photons traversed from each system. To account for the reflection of one of the two paths in the beamsplitter, we set a phase difference of $\frac{\pi}{2}$ between $|1,0\rangle$ and $|0,1\rangle$ states.

We then obtain the entangled state upon detection of a single photon

$$\begin{aligned}|\Psi_{1,2}\rangle = \frac{1}{\sqrt{2}}[|1,0\rangle \sum_{\omega} \xi_{\mathrm{Yb},\omega} \frac{\mathrm{c}^{\dagger}_{\omega} + i\,\mathrm{d}^{\dagger}_{\omega}}{\sqrt{2}} |\mathrm{vac}\rangle \\ - ie^{i\Delta\phi} |0,1\rangle \sum_{\omega'} \xi_{\mathrm{In},\omega'} \frac{\mathrm{d}^{\dagger}_{\omega'} + i\,\mathrm{c}^{\dagger}_{\omega'}}{\sqrt{2}} |\mathrm{vac}\rangle]\end{aligned} \tag{6.7}$$

The density matrix can then be computed. Let us first assume the photon was detected on path D, and not on path C. Tracing over photon states in the path D, and over all photon frequencies ω, we obtain

$$\begin{aligned}\rho^{\mathrm{Yb,In,D}} = \frac{1}{4}[\sum_{\omega} \xi^{*}_{\mathrm{Yb},\omega}\xi_{\mathrm{Yb},\omega} |1,0\rangle \langle 1,0| \\ + \sum_{\omega} \xi^{*}_{\mathrm{Yb},\omega}\xi_{\mathrm{Yb},\omega} |0,1\rangle \langle 0,1| \\ - ie^{i\Delta\phi} \sum_{\omega} \xi^{*}_{\mathrm{Yb},\omega}\xi_{\mathrm{In},\omega} |0,1\rangle \langle 1,0| \\ + ie^{-i\Delta\phi} \sum_{\omega} \xi^{*}_{\mathrm{In},\omega}\xi_{\mathrm{Yb},\omega} |1,0\rangle \langle 0,1|]\end{aligned} \tag{6.8}$$

The same matrix can be found for the path C. Summing the density matrices we then find the complete density matrix including paths C and D

$$\begin{aligned}\rho^{\mathrm{Yb,In}} = \frac{1}{2}(|1,0\rangle \langle 1,0| + |0,1\rangle \langle 0,1| \\ - ie^{i\Delta\phi} \langle \zeta_{\mathrm{Yb}} | \zeta_{\mathrm{In}} \rangle |0,1\rangle \langle 1,0| \\ + ie^{-i\Delta\phi} \langle \zeta_{\mathrm{In}} | \zeta_{\mathrm{Yb}} \rangle |1,0\rangle \langle 0,1|)\end{aligned} \tag{6.9}$$

where we have used the relations

$$\langle \zeta_{\mathrm{In}} | \zeta_{\mathrm{In}} \rangle = \langle \zeta_{\mathrm{Yb}} | \zeta_{\mathrm{Yb}} \rangle = 1, \tag{6.10}$$

$$\langle \zeta_{\mathrm{Yb}} | \zeta_{\mathrm{In}} \rangle = \langle \zeta_{\mathrm{In}} | \zeta_{\mathrm{Yb}} \rangle^{*} = \sum_{\omega} \xi^{*}_{\mathrm{In},\omega}\xi_{\mathrm{Yb},\omega}. \tag{6.11}$$

Finally, we compute the fidelity using the target state $|\Psi_{\mathrm{ent}}\rangle = \frac{1}{\sqrt{2}}(|1,0\rangle - ie^{i\Delta\phi} |0,1\rangle)$ to find

$$F = \langle \Psi_{\mathrm{ent}} | \rho^{\mathrm{Yb,In}} |\Psi_{\mathrm{ent}}\rangle = \frac{1}{2}\Big[1 + Re(\langle \zeta_{\mathrm{Yb}} | \zeta_{\mathrm{In}} \rangle)\Big]. \tag{6.12}$$

Factors which affect the entanglement fidelity are photon overlap, double-excitation events, false identification of both-system excitation as a single-system excitation, and atomic recoil from the ion interacting with the excitation laser. We can account for double excitation events by tracking the non-zero probability that both qubits were excited but only one was detected. This probability is given by

$$p_{\text{double}} = [p_{1,\text{Yb}} p_{1,\text{In}} p_{2,\text{Yb}} (1 - p_{2,\text{In}})] + [p_{1,\text{Yb}} p_{1,\text{In}} p_{2,\text{In}} (1 - p_{2,\text{Yb}})] \tag{6.13}$$

where the two terms come from the probability of detecting one photon from either qubit that has decayed from its excited state. There is a phase of $\pi/2$ between these two photons as with the state in Eq. 6.9, and an additional phase factor determined by the total optical path length of the In system $\phi_{D_2} = ikD_2$. Following through the same process, we arrive at an entangled state

$$\begin{aligned} |\Psi_{1,2}\rangle = \frac{1}{\sqrt{2+c_1^2}} \Bigg[& |1,0\rangle \sum_{\omega} \xi_{\text{Yb},\omega} \frac{\mathrm{c}^\dagger_\omega + i\,\mathrm{d}^\dagger_\omega}{\sqrt{2}} |\text{vac}\rangle \\ & - i e^{i\Delta\phi} |0,1\rangle \sum_{\omega'} \xi_{\text{In},\omega'} \frac{\mathrm{d}^\dagger_{\omega'} + i\,\mathrm{c}^\dagger_{\omega'}}{\sqrt{2}} |\text{vac}\rangle] \\ & + c_1 |1,1\rangle \Bigg[\sum_{\omega} \xi_{\text{Yb},\omega} \frac{\mathrm{c}^\dagger_\omega + i\,\mathrm{d}^\dagger_\omega}{\sqrt{2}} |\text{vac}\rangle \\ & - i e^{i(\phi_{D_2})} \sum_{\omega'} \xi_{\text{In},\omega'} \frac{\mathrm{d}^\dagger_{\omega'} + i\,\mathrm{c}^\dagger_{\omega'}}{\sqrt{2}} |\text{vac}\rangle \Bigg] \Bigg] \end{aligned} \tag{6.14}$$

where we have that

$$\begin{aligned} c_1 &= \frac{\sqrt{p_{double}}}{\sqrt{p_{1,\mathrm{Yb}}(1-p_{1,\mathrm{In}})p_{2,\mathrm{Yb}}}} \\ &= \frac{\sqrt{p_{1,\mathrm{In}}(p_{2,\mathrm{Yb}}(1-p_{2,\mathrm{In}})+p_{2,\mathrm{In}}(1-p_{2,\mathrm{Yb}}))}}{\sqrt{(1-p_{1,\mathrm{In}})p_{2,\mathrm{Yb}}}}. \end{aligned} \tag{6.15}$$

Since the target state has no $|1,1\rangle$ component, when we calculate the fidelity, we obtain the same result as before, with the only modification being the prefactor $\frac{1}{\sqrt{2}} \to \frac{1}{\sqrt{2+c_1^2}}$.

Including the effect of F_{dyn} from Cabrillo *et al.*[10] on photon distinguishibility, we then obtain the final fidelity equation:

$$F = \frac{1}{2+c_1^2}(1+F_{\mathrm{dyn}}\mathrm{Re}(\langle\zeta_{\mathrm{Yb}}\,|\,\zeta_{\mathrm{In}}\rangle). \tag{6.16}$$

It is clear from Eq. 6.16 that there is a trade-off between excitation probability and fidelity (Fig. 6.3) for this single photon entanglement scheme. If we assume perfect overlap and equal excitation probabilities for the two systems, we see that the maximum possible fidelity at 1% excitation is 97.3%. At 5% excitation, it has dropped to 94.6%, and 10% excitation has a maximal fidelity of only 91.1%. Two photon entanglement schemes wouldn't have this issue, but the short pulses required would make pulse shaping difficult, if not impossible for our systems.

6.3 Photon Collection

Photon collection efficiency primarily affects the protocol's probability of success. For trapped ions, light collection is challenging due to the high-vacuum environment and the need to isolate ions from decoherence-inducing surfaces. Typical light collection efficiency is 2-4% utilizing off-the-shelf long working distance microscope objectives [37], while optics based on in-vacuum lenses [38] and custom high-NA objectives [39] are capable of collecting up to 10% of the emitted photons. Further enhancement is possible by integrating a metallic parabolic mirror as an RF electrode of the ion trap [17]. Ions are trapped at the focus of the mirror, so that the emitted photons are collimated upon reflection from the mirror with an expected 32% overall coupling efficiency into a single-mode optical fiber. As we show below, the parabolic mirror trap also provides a novel

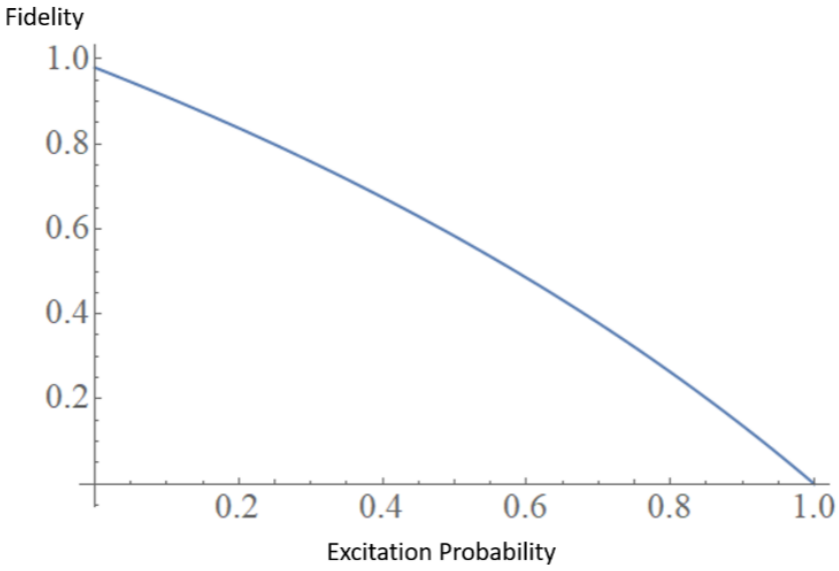

Figure 6.3: Maximum fidelity decreases with increasing excitation probability as double excitation events become more prevalent. Graph above is for perfect overlap end equal excitation probability for the two systems.

mechanism for polarization filtering. Longer term, integrated-photonics platforms may provide a path toward high-NA collection from scalable arrays of ions [40].

For the donor, a photonic cavity can be fabricated in ZnO to enhance collection efficiency. As shown in Fig. 6.4, cavities which satisfy high cooperativity $C = g^2/\kappa\Gamma_{\mathrm{In}}$ (here g is the donor-cavity coupling strength, κ is the cavity decay rate and Γ_{In} is the spontaneous decay rate) in the "bad cavity" limit necessary for the pulse-shaping procedure described below, lie in a band of readily achievable Q/V ratios with today's nanophotonic fabrication techniques. Due to intrinsic band-edge absorption, the high quality factor region in Fig. 6.4 may not be achievable at D^0X-D^0 transition [41], thus low mode volume cavities with moderate quality factors should be targeted. While nanophotonic fabrication in ZnO is relatively immature compared to other quantum defect host crystals, small mode volume ZnO nanowire cavities have enabled UV lasers [42] and ZnO cavities fabricated by focused ion beam milling [43], a method that has been used to achieve high cooperativity in rare-earth doped systems [44], exhibit quality factors up to 1000. In the limit that

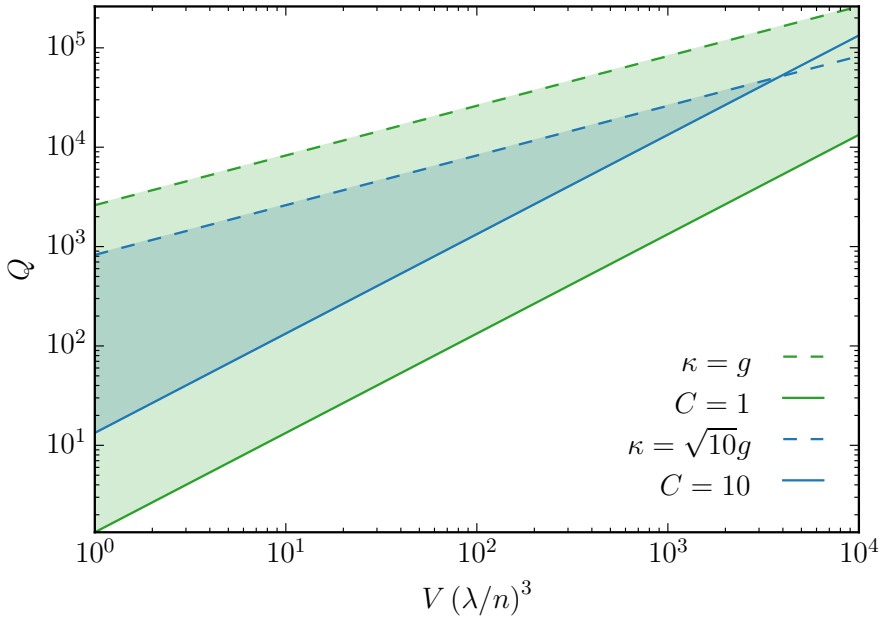

Figure 6.4: ZnO cavity parameter space (κ, g, C) satisfying the photon pulse-shaping requirements in terms of the quality factor Q and the mode volume V. The green area corresponds to $C \geq 1$ and $g \leq \kappa$, and the blue area corresponds to $C \geq 10$ and $\sqrt{10}g \leq \kappa$. *Image credit: Vasilis Niaouris*

the cavity photon loss rate κ is dominated by coupling to the output mode, over 50% collection efficiency into a waveguide for planar geometry cavities [45] or into an objective lens for nanowire cavities [46] is possible.

6.4 Photon Indistinguishability

6.4.1 Frequency

As shown in Eq. 6.16, for high fidelity entanglement, the frequency, polarization, and temporal shape of the photons emitted by the two systems must be matched to maximize $\Re(\langle\zeta_{\mathrm{Yb}}\,|\,\zeta_{\mathrm{In}}\rangle)$. The type of donor used affects the amount of frequency shift required to match the emission frequency of Yb^+. Of the three primary donor candidates, Al, Ga and In, the In D^0X transition is closest to the Yb^+ transition, $\nu_{\mathrm{In}} = \nu_{\mathrm{Yb}} + 0.34$ THz [47]. The donor will be integrated in an optical cavity detuned from the relevant transition by $\sim$200 GHz. The remaining frequency shift will be attained

via the dc Stark effect. Electric field tuning in a similar quantum dot trion system has shown that several meV of tuning is possible [48].

6.4.2 Polarization

Decay from $|\mathrm{e}\rangle_{\mathrm{Yb}}$ ($^2P_{1/2}$ $|F=1,m_F=0\rangle$) can occur along three different channels, producing either a $\sigma^{\pm}$ Raman photon or a π Rayleigh photon (see Fig.6.1). A pure polarization state is required for polarization matching with the photon emitted by the ZnO donor. While the use of a high-NA collection optic increases the photon collection efficiency, it can pose problems for polarization purity. However, the parabolic mirror can be utilized to filter out the undesired π polarized photons when the optical axis is oriented along the quantization axis defined by the applied magnetic field [20]. In this geometry, the π-polarized photons reflected off the mirror have a radial polarization pattern, which completely destructively interferes when focused into a single-mode optical fiber. The σ-polarized photons, on the other hand, have an elliptical polarization upon reflection from the mirror. The eccentricity increases with radial distance from the center, with perfectly circular polarization at the center of the reflected beam and linear polarization at the edge. The linear component is filtered out by destructive interference in the optical fiber.

In the Voigt geometry, with the applied magnetic field perpendicular to the crystal axis, the branching ratio between the ZnO donor Raman transitions $|\mathrm{e}\rangle_{\mathrm{In}} \rightarrow |0\rangle_{\mathrm{In}}$ and $|\mathrm{e}\rangle_{\mathrm{In}} \rightarrow |1\rangle_{\mathrm{In}}$ is approximately 1:1 [49, 50]. For a cavity with large V and high Q (e.g. ring resonator [51]), the cavity resonance will be narrower than the Zeeman splitting of D^0, allowing for selective coupling of the desired Raman transition. For high V, the size of the cavity is large compared to the excitation beam diameter, so polarization selection can be attained by selectively exciting a small area of the cavity, where only one dipole moment is coupled to the cavity mode. For cavities with low Q and V, polarization and frequency selection can be achieved via cross polarization [36], waveguide excitation [52] and spectral filtering.

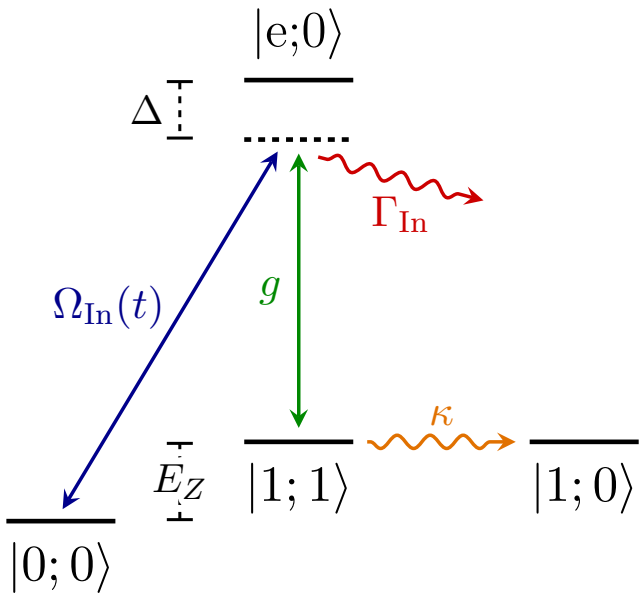

Figure 6.5: ZnO energy-level system used in pulse-shaping calculations. The kets represent the In:ZnO state and the associated photon number.

6.4.3 Temporal Shape

Matching the temporal profiles of the emitted photons poses a greater challenge. The $^2P_{1/2}$ Yb^+ state lifetime is 8.1 ns [53], while that of D^0X state in ZnO is only 1.4 ns [54]. Post-emission pulse shaping [55, 56] is not feasible because the ZnO and Yb photons are too narrow band for these dispersive methods. Instead, the photons emitted by the ZnO donor can be pulse-shaped at their creation [57] by modulating the intensity of the excitation pulse. The ZnO cavity is constructed with parameters within the “bad cavity" regime ($\kappa \gg g^2/\kappa \gg \Gamma_{\text{In}}$) [57]. The large cavity decay rate ensures that we are not in the strong coupling regime, so the donor excitation follows the optical pulse, while the high cooperativity ensures that the donor decays via Raman emission into the cavity.

6.5 Performance

While it is possible to obtain an analytic expression for the ideal excitation pulse shape for maximum photon overlap [58], in this work we limit ourselves to experimentally attractive Gaussian pulses and performed numerical simulations to determine photon temporal overlap, given the practical cavity considerations discussed above. The donor defect is modeled as a three level system with initial state $|0\rangle_{\mathrm{In}}$ (Fig. 6.5) connected to the excited state $|\mathrm{e}\rangle_{\mathrm{In}}$ by an excitation pulse of Rabi frequency $\Omega_{\mathrm{In}}(t)$ and detuning Δ. We neglect the effect of the other excited state level. The cavity is coupled to the $|e;0\rangle \leftrightarrow |1;1\rangle$ transition with detuning Δ and coupling strength g. Photons from this transition have a spontaneous radiative decay rate of Γ_{In}. Photons escape the cavity at the cavity decay rate κ. The equations of motion for the population amplitudes are [57, 58]

$$i\frac{d}{dt}a_{\mathrm{In}}(t) = \frac{1}{2}\begin{pmatrix} 0 & \Omega_{\mathrm{In}}(t) & 0 \\ \Omega^{*}{}_{\mathrm{In}}(t) & 2\Delta - i\Gamma_{\mathrm{In}} & 2g \\ 0 & 2g & -i\kappa \end{pmatrix} a_{\mathrm{In}}(t), \tag{6.17}$$

where $a_{\mathrm{In}}(t) = [a_{0,\mathrm{In}}(t), a_{\mathrm{e,In}}(t), a_{1,\mathrm{In}}(t)]^T$.

The Yb^+ is modeled in a similar manner but without a cavity. The ground state $|0\rangle_{\mathrm{Yb}}$ is coupled to the excited state $|\mathrm{e}\rangle_{\mathrm{Yb}}$ by the Rabi pulse $\Omega_{\mathrm{Yb}}(t)$. Decay from the excited state occurs with the rate Γ_{Yb}. The equations of motion are:

$$i\frac{d}{dt}\begin{pmatrix} a_{0,\mathrm{Yb}}(t) \\ a_{\mathrm{e,Yb}}(t) \end{pmatrix} = \frac{1}{2}\begin{pmatrix} 0 & \Omega_{\mathrm{Yb}}(t) \\ \Omega^{*}{}_{\mathrm{Yb}}(t) & -i\Gamma_{\mathrm{Yb}} \end{pmatrix}\begin{pmatrix} a_{0,\mathrm{Yb}}(t) \\ a_{\mathrm{e,Yb}}(t) \end{pmatrix} \tag{6.18}$$

The emission rates of the photons from the ZnO and Yb^+ systems are $\kappa|a_{1,\mathrm{In}}(t)|^2$ and $\Gamma_{\mathrm{Yb}}|a_{e,\mathrm{Yb}}(t)|^2$, respectively [57], with temporal wavefunctions given by normalizing the population amplitudes $a_{1,\mathrm{In}}(t) \rightarrow A_{1,\mathrm{In}}(t)$ and $a_{\mathrm{e,Yb}}(t) \rightarrow A_{\mathrm{e,Yb}}(t)$. By controlling the Rabi frequencies $\Omega_{\mathrm{In}}(t)$ and $\Omega_{\mathrm{Yb}}(t)$, it is possible to engineer the real component of the photon overlap $\int_{-\infty}^{\infty} A^{*}_{e,\mathrm{Yb}}(t)A_{1,\mathrm{In}}(t)dt = \langle \zeta_{\mathrm{Yb}} \,|\, \zeta_{\mathrm{In}} \rangle$ to ~0.99 for practical experimental parameters using the control pulses shown in Fig. 6.6 for a system with $\sim$5% excitation. The optimized pulse is restricted to a Gaussian pulse shape with adjustable rise time σ_1, fall time σ_2, time to pulse max τ, hold time t_h, maximum pulse height Ω_{max},

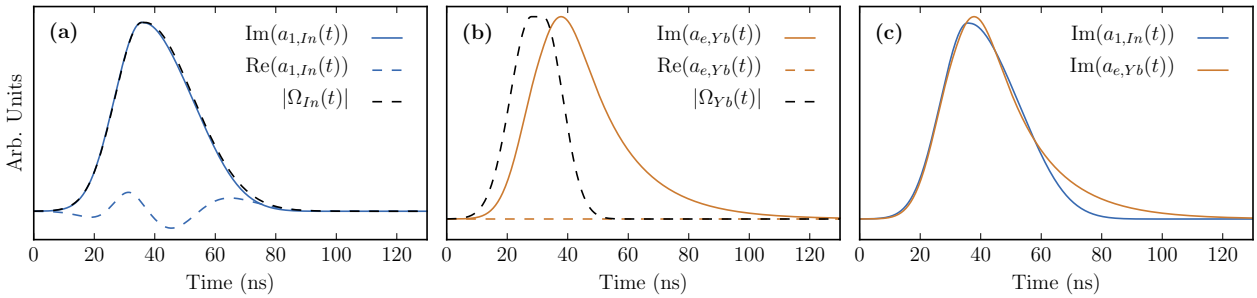

Figure 6.6: (a) Excitation pulse and temporal wavefunction of the emitted photon for the ZnO system with approximately 5% emission for the donor and ion. The parameters used are $\Delta = 2\pi\times(200\,\text{GHz})$, $\sigma_1 = 8.9\,\text{ns}$, $\sigma_2 = 16\,\text{ns}$, $\tau = 35.8\,\text{ns}$, $t_h = 0.85\,\text{ns}$, $\Omega_{max} = 2\pi\times(2.9\,\text{GHz})$, $\theta_1 = 2\pi\times(6.9\ \text{MHz})$, $\theta_0 = 2\pi\times(-0.15)$, $g = 2\pi\times(15\,\text{GHz})$, and $\kappa = 2\pi\times(60\,\text{GHz})$. (b) Excitation pulse and temporal wavefunction of emitted photon for the Yb^+ system with $\sigma_1 = 7.0\,\text{ns}$, $\sigma_2 = 6.4\,\text{ns}$, $\tau = 28\,\text{ns}$, $t_h = 3.9\,\text{ns}$, $\Omega_{max} = 2\pi\times(8.1\,\text{MHz})$, $\theta_1 = 0$ GHz, and $\theta_0 = 2\pi\times(0.50)$. (c) Imaginary parts of both wavefunctions, leading to $\text{Re}(\langle\zeta_{\text{Yb}}\,|\,\zeta_{\text{In}}\rangle) \simeq 0.99$.

and phase factor $e^{i\alpha(t)}$ where $\alpha(t) = \theta_0 + \theta_1 t$ describes a linear time-dependent phase. Setting either pulse to achieve a desired excitation probability $p_{1,x}$, we iteratively sweep the pulse parameters for the other system to obtain local maxima in the overlap.

The probability of successful entanglement is

$$P_{\text{succ}} = [p_{1,\text{Yb}}p_{2,\text{Yb}}(1-p_{1,\text{In}}) + p_{1,\text{In}}p_{2,\text{In}}(1-p_{1,\text{Yb}})]\eta \tag{6.19}$$

where $p_{2,x}$ is the collection efficiency from each system and η is the quantum efficiency of the detector, which can be as high as ~80% using superconducting nanowire single photon detectors (SNSPD's) [59] for photons at 369 nm. With a parabolic mirror ion trap, collection efficiency for Yb^+ systems is 32%; the collection efficiency of the ZnO system is set according to Eq. 6.3 such that collected photons have equal probability of originating from either system. Excitation probabilities depend on the pulse shaping requirements, and need to be kept low (<10%) to minimize error (Table 6.1).

Each experimental run begins with ~1 μs of optical pumping, followed by the ~10 ns excitation pulse. If a single photon is detected, then the state readout is performed, taking ~10 μs and limited by the ion [59]. For ~5% excitation, we find a success probability of ~2.7%, leading to

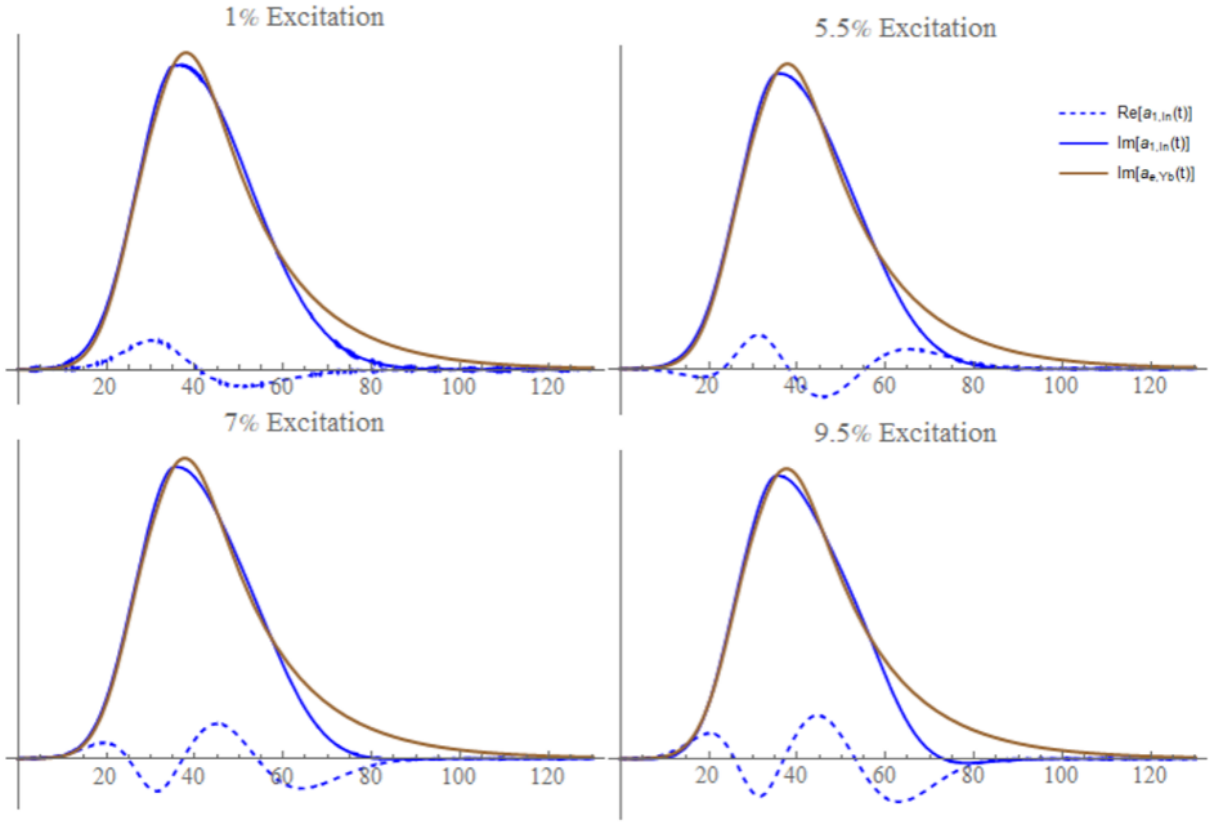

Figure 6.7: Stronger excitation pulses increase the real component of $a_{1,In}(t)$. This decreases the real component of the overlap, which is proportional to the fidelity of the final entangled state.

In Excitation	Yb Excitation	Overlap	Fidelity	Probability of Success
1.1%	1.0%	0.992	96.9%	0.5%
5.4%	5.5%	0.989	93.9%	2.7%
7.1%	6.9%	0.985	92.5%	3.3%
9.7%	9.6%	0.975	90.2%	4.4%

Table 6.1: With pulse shaping limited to a simple linear function in phase, maximal overlap decreases at higher excitation probabilities, as does fidelity of the final entangled state. The probability of success increases with increased excitation, but given the drop in fidelity it was determined that an excitation probability of approximately 5% is desired.

an entanglement generation rate of 21 kHz. Practically, this rate will be further decreased by the interferometer phase stabilization and defect frequency stabilization steps [60].

With all experiments using this type of protocol, there is a tradeoff between success probability and fidelity [61, 60]. One can always increase the success probability by increasing the excitation probability, but this degrades the fidelity according to Eq 6.16 (Fig. 6.3). Further, in order to be useful, the entanglement rate needs to be comparable to the rate of decoherence. While the demonstrated coherence time for trapped ytterbium ions is long [62] (10 minutes), the spin echo time T_2 of ensemble donor bound excitons in ZnO is only 50 μs. However, the fundamental limit of T_2 is the longitudinal spin relaxation time T_1 which exceeds 100 ms [49] and may allow for improvement through chemical and isotope purification [63].

6.6 Conclusion

In summary, a ZnO donor defect qubit and a single trapped Yb^+ ion can be remotely entangled via a photonic link at 369 nm. Pulse shaping techniques can be used to alter the temporal profile of the photon emitted by the donor to attain the temporal wavefunction overlap of 0.99 with the photon emitted by the trapped ion, leading to an entangled state fidelity of 94% with realistic parameters at 5% excitation.

Chapter 7

FUTURE DIRECTIONS - QUANTUM JUMPS

In 2019, Minev *et al.* published results of an experiment utilizing a superconducting artificial 3-level atom to examine quantum jumps[1]. The system was strongly driven to a 'bright' state, and the population of that state was continuously measured (see Fig. 7.2 for analogous barium levels). Once the expected time between transitions was established, the system was also weakly driven to the 'dark' state. The transitions from the bright state continued to be measured, and it was discovered that there is a latency period before a jump to the dark state occurs. This allowed the researchers to determine when a jump was about to occur and then 'catch and reverse' the quantum jump.

We intend to recreate this experiment using a trapped barium ion. This will confirm the behavior on another quantum system and inform on the behavior of ions when undergoing quantum jumps. Light collection is the primary challenge to performing this experiment with a trapped ion. With their superconducting system, Minev *et al.* is able to detect nearly every transition, while trapped ion systems tend to have collection efficiencies below 10%. Without high collection, it

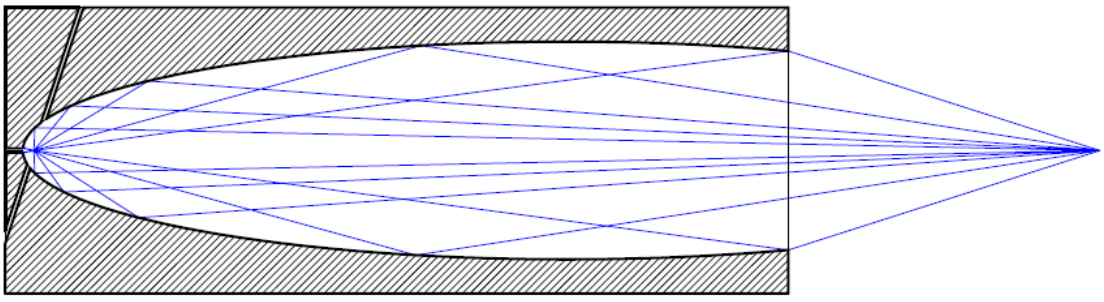

Figure 7.1: Schematic of proposed ellipsoidal mirror trap. Light from 95% of the solid angle surrounding the ion would be sent to the detection pathway.

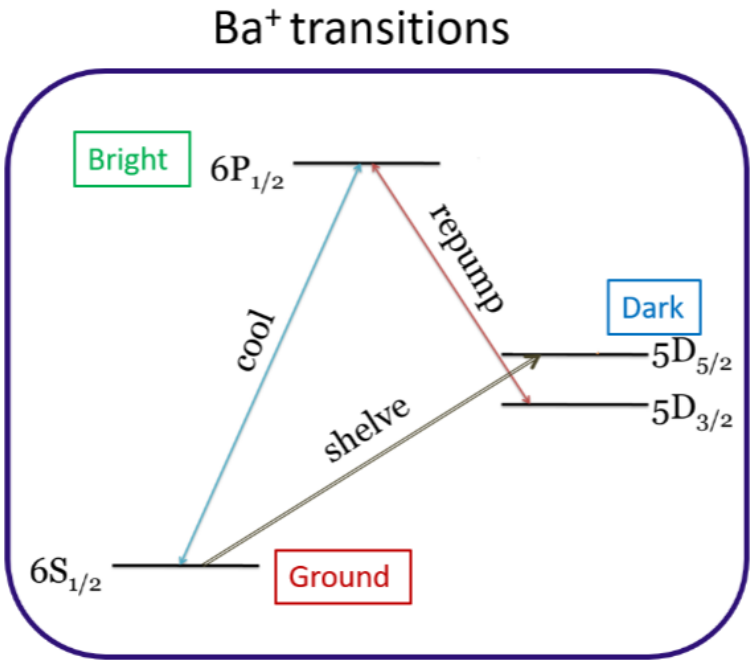

Figure 7.2: Selected energy levels of $^{138}Ba^{+}$. For quantum jumps observation, we strongly drive the ground to bright transition and collect the 369 nm photons which emit while weakly encouraging transitions to the dark state, $5D_{5/2}$. We detect a quantum jump to the dark state by the absence of 493 nm photons from the bright transition.

will be difficult to detect the latency period before a jump occurs.

We have received funding for the construction of a ellipsoidal mirror trap capable of collecting light from 95% of the solid angle around an ion trapped at the focus (Fig. 7.1), and intend to use this system to study quantum jumps in a trapped barium ion using the levels displayed in Figure 7.2. The first step of this experiment will be to determine the photon collection rate of the system when driving the $6S_{1/2}$ to $6P_{1/2}$ (bright) transition. This is accomplished through illumination with a 493 nm beam. The bright state has a lifetime of 7.8 ns, and two common decay channels; to ground (75.6%) or $5D_{3/2}$ (24.4%), a dark state with lifetime of seconds. This transition will also need to be strongly driven with a repump beam of 650 nm.

If light collection per solid angle follows what we measured with the parabolic mirror trap, we can expect to detect a photon every 0.09 μs when driving the bright transition at saturation intensity

in the ellipsoidal mirror trap. Latency periods in the superconducting atom were found to be 2 μs, but the lifetime of the excited state we're using is very short (7.8 ns), which will likely decrease the latency period to something on the scale of nanoseconds.

Once the expected photon count rate has been established, we can begin to examine quantum jumps in the same manner as Minev *et al*. This will be accomplished by driving the dark transition weakly with a 1762 nm laser while still strongly driving the system with 493 nm and 650 nm beams. Filters in the optical pathway will ensure that only 493 nm photons are collected. Photon arrival times will be monitored, and when a longer than expected period of time passes without detecting a photon, if will be taken as a sign that a quantum jump has begun to occur. At this point, the 493 nm laser will be turned off and a $\pi/2$ pulse applied with the 1762 nm laser. Assuming that we caught a jump and the ion was somewhere between the ground and dark state, this would drive the transition to completion in the dark state. If jumps are instantaneous, the system would be in either ground or dark when the pulse was applied, leading to a 50/50 superposition of ground and dark states after the pulse was applied. A $3\pi/2$ pulse could be used instead to drive the system to ground instead of dark.

After the Rabi pulse has been applied, the state of the ion will be read out. Measurement statistics built up from repeated experiments will reveal how successfully we were able to detect the jump.

Additionally, a time to digital converter will be used to examine photon arrival times. A PicoHarp has picosecond resolution time-correlated single photon counting which can reconstruct the temporal profile of emitted single photons with reference to the exciting laser pulse. The first will be an examination of the temporal profile of photons which arrive just before or after a jump occurs. Any difference in the photon profiles will add to our jump-predicting capabilities.

BIBLIOGRAPHY

[1] Z. K. Minev, S. O. Mundhada, S. Shankar, P. Reinhold, R. Gutiérrez-Jáuregui, R. J. Schoelkopf, M. Mirrahimi, H. J. Carmichael, and M. H. Devoret, "To catch and reverse a quantum jump mid-flight," *Nature*, vol. 570, no. 7760, pp. 200–204, 2019.

[2] N. Kurz, *Experiments with remote entanglement using single barium ions*. University of Washington, 2010.

[3] W. Paul, "Electromagnetic traps for charged and neutral particles," *Reviews of modern physics*, vol. 62, no. 3, p. 531, 1990.

[4] T. Aragona, *Piezoelectric Deformable Mirrors*, 2014 (accessed July 25, 2020). https://www.thorlabs.com/newgrouppage9.cfm?objectgroup$_id = 5056pn = DMP40 - P01$.

[5] A. Steele, L. Churchill, P. Griffin, and M. Chapman, "Photoionization and photoelectric loading of barium ion traps," *Physical Review A*, vol. 75, no. 5, p. 053404, 2007.

[6] M. H. Devoret, A. Wallraff, and J. M. Martinis, "Superconducting qubits: A short review," *arXiv preprint cond-mat/0411174*, 2004.

[7] C. Nayak, S. H. Simon, A. Stern, M. Freedman, and S. D. Sarma, "Non-abelian anyons and topological quantum computation," *Reviews of Modern Physics*, vol. 80, no. 3, p. 1083, 2008.

[8] N. Bohr, "Xxxvii. on the constitution of atoms and molecules," *The London, Edinburgh, and Dublin Philosophical Magazine and Journal of Science*, vol. 26, no. 153, pp. 476–502, 1913.

[9] W. Nagourney, J. Sandberg, and H. Dehmelt, "Shelved optical electron amplifier: Observation of quantum jumps," *Physical Review Letters*, vol. 56, no. 26, p. 2797, 1986.

[10] C. Cabrillo, J. I. Cirac, P. Garcia-Fernandez, and P. Zoller, "Creation of entangled states of distant atoms by interference," *Physical Review A*, vol. 59, no. 2, p. 1025, 1999.

[11] S. Earnshaw, "On the nature of the molecular forces which regulate the constitution of the luminiferous ether," *TCaPS*, vol. 7, p. 97, 1848.

[12] D. Berkeland, J. Miller, J. C. Bergquist, W. M. Itano, and D. J. Wineland, "Minimization of ion micromotion in a paul trap," *Journal of applied physics*, vol. 83, no. 10, pp. 5025–5033, 1998.

[13] P. L. W. Maunz, "High optical access trap 2.0.," tech. rep., Sandia National Lab.(SNL-NM), Albuquerque, NM (United States), 2016.

[14] M. Ivory, A. Kato, A. Hasanzadeh, and B. Blinov, "A paul trap with sectored ring electrodes for experiments with two-dimensional ion crystals," *Review of Scientific Instruments*, vol. 91, no. 5, p. 053201, 2020.

[15] F. Diedrich, J. Bergquist, W. M. Itano, and D. Wineland, "Laser cooling to the zero-point energy of motion," *Physical Review Letters*, vol. 62, no. 4, p. 403, 1989.

[16] G. Shu, C.-K. Chou, N. Kurz, M. R. Dietrich, and B. B. Blinov, "Efficient fluorescence collection and ion imaging with the "tack" ion trap," *JOSA B*, vol. 28, no. 12, pp. 2865–2870, 2011.

[17] C.-K. Chou, C. Auchter, J. Lilieholm, K. Smith, and B. Blinov, "Note: Single ion imaging and fluorescence collection with a parabolic mirror trap," *Review of Scientific Instruments*, vol. 88, no. 8, p. 086101, 2017.

[18] N. Lindlein, R. Maiwald, H. Konermann, M. Sondermann, U. Peschel, and G. Leuchs, "A new 4π geometry optimized for focusing on an atom with a dipole-like radiation pattern," *Laser Physics*, vol. 17, no. 7, pp. 927–934, 2007.

[19] R. Maiwald, A. Golla, M. Fischer, M. Bader, S. Heugel, B. Chalopin, M. Sondermann, and G. Leuchs, "Collecting more than half the fluorescence photons from a single ion," *Physical Review A*, vol. 86, no. 4, p. 043431, 2012.

[20] T. Kim, P. Maunz, and J. Kim, "Efficient collection of single photons emitted from a trapped ion into a single-mode fiber for scalable quantum-information processing," *Physical Review A*, vol. 84, no. 6, p. 063423, 2011.

[21] L. Luo, D. Hayes, T. Manning, D. Matsukevich, P. Maunz, S. Olmschenk, J. Sterk, and C. Monroe, "Protocols and techniques for a scalable atom–photon quantum network," *Fortschritte der Physik*, vol. 57, no. 11-12, pp. 1133–1152, 2009.

[22] J. D. Siverns, J. Hannegan, and Q. Quraishi, "Neutral-atom wavelength-compatible 780 nm single photons from a trapped ion via quantum frequency conversion," *Phys. Rev. Applied*, vol. 11, p. 014044, Jan 2019.

[23] S. Zaske, A. Lenhard, C. A. Keßler, J. Kettler, C. Hepp, C. Arend, R. Albrecht, W.-M. Schulz, M. Jetter, P. Michler, *et al.*, "Visible-to-telecom quantum frequency conversion of light from a single quantum emitter," *Physical review letters*, vol. 109, no. 14, p. 147404, 2012.

[24] M. Bock, P. Eich, S. Kucera, M. Kreis, A. Lenhard, C. Becher, and J. Eschner, "High-fidelity entanglement between a trapped ion and a telecom photon via quantum frequency conversion," *Nature communications*, vol. 9, no. 1, pp. 1–7, 2018.

[25] H. Rütz, K.-H. Luo, H. Suche, and C. Silberhorn, "Quantum frequency conversion between infrared and ultraviolet," *Physical Review Applied*, vol. 7, no. 2, p. 024021, 2017.

[26] M. Keller, B. Lange, K. Hayasaka, W. Lange, and H. Walther, "Continuous generation of single photons with controlled waveform in an ion-trap cavity system," *Nature*, vol. 431, no. 7012, pp. 1075–1078, 2004.

[27] L. Fan, C.-L. Zou, N. Zhu, and H. X. Tang, "Spectrotemporal shaping of itinerant photons via distributed nanomechanics," *Nature Photonics*, vol. 13, no. 5, pp. 323–327, 2019.

[28] M. Karpiński, M. Jachura, L. J. Wright, and B. J. Smith, "Bandwidth manipulation of quantum light by an electro-optic time lens," *Nature Photonics*, vol. 11, no. 1, p. 53, 2017.

[29] Y. Wang, M. Um, J. Zhang, S. An, M. Lyu, J.-N. Zhang, L.-M. Duan, D. Yum, and K. Kim, "Single-qubit quantum memory exceeding ten-minute coherence time," *Nature Photonics*, vol. 11, no. 10, pp. 646–650, 2017.

[30] N. M. Linke, D. Maslov, M. Roetteler, S. Debnath, C. Figgatt, K. A. Landsman, K. Wright, and C. Monroe, "Experimental comparison of two quantum computing architectures," *Proceedings of the National Academy of Sciences*, vol. 114, no. 13, pp. 3305–3310, 2017.

[31] R. J. Warburton, "Single spins in self-assembled quantum dots," *Nature materials*, vol. 12, no. 6, pp. 483–493, 2013.

[32] K.-M. C. Fu, S. M. Clark, C. Santori, C. R. Stanley, M. Holland, and Y. Yamamoto, "Ultrafast control of donor-bound electron spins with single detuned optical pulses," *Nature Physics*, vol. 4, no. 10, pp. 780–784, 2008.

[33] Y. He, S. K. Gorman, D. Keith, L. Kranz, J. G. Keizer, and M. Y. Simmons, "A two-qubit gate between phosphorus donor electrons in silicon," *Nature*, vol. 571, no. 7765, pp. 371–375, 2019.

[34] B. E. Kane, "A silicon-based nuclear spin quantum computer," *Nature*, vol. 393, no. 6681, pp. 133–137, 1998.

[35] E. Waks and C. Monroe, "Protocol for hybrid entanglement between a trapped atom and a quantum dot," *Physical Review A*, vol. 80, no. 6, p. 062330, 2009.

[36] H. Meyer, R. Stockill, M. Steiner, C. Le Gall, C. Matthiesen, E. Clarke, A. Ludwig, J. Reichel, M. Atatüre, and M. Köhl, "Direct photonic coupling of a semiconductor quantum dot and a trapped ion," *Physical review letters*, vol. 114, no. 12, p. 123001, 2015.

[37] B. Blinov, D. Moehring, L.-M. Duan, and C. Monroe, "Observation of entanglement between a single trapped atom and a single photon," *Nature*, vol. 428, p. 153–157, 2004.

[38] G. Araneda, D. Higginbottom, L. Slodička, Y. Colombe, and R. Blatt, "Interference of single photons emitted by entangled atoms in free space," *Physical Review Letters*, vol. 120, p. 193603, 2018.

[39] L. Stephenson, D. Nadlinger, B. Nichol, S. An, P. Drmota, T. Ballance, K. Thirumalai, J. Goodwin, D. Lucas, and C. Ballance, "High-rate, high-fidelity entanglement of qubits across an elementary quantum network," *Physical Review Letters*, vol. 124, no. 11, p. 110501, 2020.

[40] C. D. Bruzewicz, J. Chiaverini, R. McConnell, and J. M. Sage, "Trapped-ion quantum computing: Progress and challenges," *Applied Physics Reviews*, vol. 6, no. 2, p. 021314, 2019.

[41] S. Nur, H.-J. Lim, J. Elzerman, and J. J. L. Morton, "Silicon photonic crystal cavities at near band-edge wavelengths," *Applied Physics Letters*, vol. 114, no. 9, p. 091101, 2019.

[42] M. H. Huang, S. Mao, H. Feick, H. Yan, Y. Wu, H. Kind, E. Weber, R. Russo, and P. Yang, "Room-temperature ultraviolet nanowire nanolasers," *Science*, vol. 292, no. 5523, pp. 1897–1899, 2001.

[43] T.-C. Chang, K.-B. Hong, Y.-Y. Lai, Y.-H. Chou, S.-C. Wang, and T.-C. Lu, "Zno-based microcavities sculpted by focus ion beam milling," *Nanoscale Research Letters*, vol. 11, no. 1, p. 319, 2016.

[44] T. Zhong, J. M. Kindem, J. G. Bartholomew, J. Rochman, I. Craiciu, V. Verma, S. W. Nam, F. Marsili, M. D. Shaw, A. D. Beyer, and A. Faraon, "Optically addressing single rare-earth ions in a nanophotonic cavity," *Phys. Rev. Lett.*, vol. 121, p. 183603, Oct 2018.

[45] M. Arcari, I. Söllner, A. Javadi, S. Lindskov Hansen, S. Mahmoodian, J. Liu, H. Thyrrestrup, E. H. Lee, J. D. Song, S. Stobbe, and P. Lodahl, "Near-unity coupling efficiency of a quantum emitter to a photonic crystal waveguide," *Phys. Rev. Lett.*, vol. 113, p. 093603, Aug 2014.

[46] P. Senellart, G. Solomon, and A. White, "High-performance semiconductor quantum-dot single-photon sources," *Nature Nanotechnology*, vol. 12, no. 11, pp. 1026–1039, 2017.

[47] B. Meyer, H. Alves, 1, D. Hofmann, W. Kriegseis, D. Forster, F. Bertram, J. Christen, A. Hoffmann, M. Straßburg, M. Dworzak, *et al.*, "Bound exciton and donor–acceptor pair recombinations in ZnO," *physica status solidi (b)*, vol. 241, no. 2, pp. 231–260, 2004.

[48] A. J. Bennett, R. B. Patel, J. Skiba-Szymanska, C. A. Nicoll, I. Farrer, D. A. Ritchie, and A. J. Shields, "Giant stark effect in the emission of single semiconductor quantum dots," *Applied Physics Letters*, vol. 97, no. 3, p. 031104, 2010.

[49] X. Linpeng, M. L. Viitaniemi, A. Vishnuradhan, Y. Kozuka, C. Johnson, M. Kawasaki, and K.-M. C. Fu, "Coherence properties of shallow donor qubits in zn o," *Physical Review Applied*, vol. 10, no. 6, p. 064061, 2018.

[50] M. R. Wagner, J.-H. Schulze, R. Kirste, M. Cobet, A. Hoffmann, C. Rauch, A. V. Rodina, B. K. Meyer, U. Röder, and K. Thonke, "Γ 7 valence band symmetry related hole fine splitting of bound excitons in zno observed in magneto-optical studies," *Physical Review B*, vol. 80, no. 20, p. 205203, 2009.

[51] X. Liu, A. W. Bruch, Z. Gong, J. Lu, J. B. Surya, L. Zhang, J. Wang, J. Yan, and H. X. Tang, "Ultra-high-Q UV microring resonators based on a single-crystalline aln platform," *Optica*, vol. 5, no. 10, pp. 1279–1282, 2018.

[52] T. Huber, M. Davanco, M. Müller, Y. Shuai, O. Gazzano, and G. S. Solomon, "Filter-free single-photon quantum dot resonance fluorescence in an integrated cavity-waveguide device," *Optica*, vol. 7, no. 5, pp. 380–385, 2020.

[53] S. Olmschenk, D. Hayes, D. Matsukevich, P. Maunz, D. Moehring, K. Younge, and C. Monroe, "Measurement of the lifetime of the 6p $^2P_{1/2}$ level of Yb^+," *Physical Review A*, vol. 80, no. 2, p. 022502, 2009.

[54] M. Wagner, G. Callsen, J. Reparaz, J.-H. Schulze, R. Kirste, M. Cobet, I. Ostapenko, S. Rodt, C. Nenstiel, M. Kaiser, *et al.*, "Bound excitons in ZnO: Structural defect complexes versus shallow impurity centers," *Physical Review B*, vol. 84, no. 3, p. 035313, 2011.

[55] L. J. Wright, M. Karpiński, C. Söller, and B. J. Smith, "Spectral shearing of quantum light pulses by electro-optic phase modulation," *Physical review letters*, vol. 118, no. 2, p. 023601, 2017.

[56] S.-Y. Baek, O. Kwon, and Y.-H. Kim, "Temporal shaping of a heralded single-photon wave packet," *Physical Review A*, vol. 77, no. 1, p. 013829, 2008.

[57] C. Law and H. Kimble, "Deterministic generation of a bit-stream of single-photon pulses," *Journal of Modern Optics*, vol. 44, no. 11-12, pp. 2067–2074, 1997.

[58] G. S. Vasilev, D. Ljunggren, and A. Kuhn, "Single photons made-to-measure," *New Journal of Physics*, vol. 12, no. 6, p. 063024, 2010.

[59] S. Crain, C. Cahall, G. Vrijsen, E. E. Wollman, M. D. Shaw, V. B. Verma, S. W. Nam, and J. Kim, "High-speed low-crosstalk detection of a $^{171}Yb^{+}$ qubit using superconducting nanowire single photon detectors," *Communications Physics*, vol. 2, p. 97, 2019.

[60] P. C. Humphreys, N. Kalb, J. P. J. Morits, R. N. Schouten, R. F. L. Vermeulen, D. J. Twitchen, M. Markham, and R. Hanson, "Deterministic delivery of remote entanglement on a quantum network," *Nature*, vol. 558, 2018.

[61] L. Slodička, G. Hétet, N. Röck, P. Schindler, M. Hennrich, and R. Blatt, "Atom-atom entanglement by single-photon detection," *Physical review letters*, vol. 110, no. 8, p. 083603, 2013.

[62] Y. Wang, M. Um, J. Zhang, S. An, M. Lyu, J.-N. Zhang, L.-M. Duan, D. Yum, and K. Kim, "Single-qubit quantum memory exceeding ten-minute coherence time," *Nature Photonics*, vol. 11, pp. 646–650, 2017.

[63] J. Tribollet, "Theory of the electron and nuclear spin coherence times of shallow donor spin qubits in isotopically and chemically purified zinc oxide," *The European Physical Journal B*, vol. 72, no. 4, p. 531, 2009.